Inferring tide-induced ephemeral grounding and subsequent dynamical response in an ice-shelf-stream system: Rutford Ice Stream, West Antarctica

Minyan Zhong[1], Mark Simons[1], Lijun Zhu[1], Brent Minchew[2]

[1]California Institute of Technology, Pasadena, CA, U.S.
[2]Massachusetts Institute of Technology, Cambridge, MA, U.S.

Key Points:

- We develop an approach to inferring tide-induced ephemeral grounding of ice shelves from synthetic-aperture radar observations.
- Ephemeral grounding plays a key role in the asymmetric response of ice-shelf flows to tidal forcing.
- Ice flow rate will increase if the ice shelf thins such that the identified ephemeral grounding zones become permanently ungrounded.

Abstract

Antarctic ice shelves play a key role in regulating the rate of flow in tributary ice streams. Temporal variations in the associated ice-shelf buttressing stress are observed to impact the flow in glaciers and ice streams. Ephemeral grounding induced by tides is considered as an important mechanism for modulating the buttressing stress. Here, we develop an approach to inferring variations in 3-D surface displacements at an ice-shelf-stream system that explicitly accounts for ephemeral grounding. Using a temporally dense 9-month long SAR image acquisition campaign collected over Rutford Ice Stream by the COSMO-SkyMed 4-satellite constellation, we infer the ephemeral grounding zones and the spatial-temporal variation of the fortnightly flow variability. Expanding on previous results, we find ephemeral grounding zones along the western ice-shelf margin as well as a few prominent ephemeral grounding points in the central trunk and in the vicinity of the grounding zone. Our observations provide evidence for tide-modulated buttressing stress and the temporally asymmetric response of ice-shelf flow to tidal forcing. Our study suggests that RIS will accelerate if the ice shelf thins sufficiently that the ephemeral grounding zones we have identified remain permanently ungrounded over the tidal cycle.

Plain Language Summary

Antarctic ice shelves, the floating extensions of Antarctic Ice Sheet, play a key role in ice-flow dynamics by providing buttressing forces that resist the seaward flow of ice. Temporal variations in buttressing forces have been observed at glaciers and ice streams to impact ice-flow speed. The grounding of ice shelves on the seafloor during low ocean tides, which is referred to as ephemeral grounding, causes temporal variations in buttressing forces but is not well understood due to a lack of suitable data. Here, we develop an approach to inferring the surface displacements at an ice-shelf-stream system that explicitly account ephemeral grounding from satellite radar observations. Using active, spaceborne radar data collected over Rutford Ice Stream, West Antarctica, we infer ephemeral grounding zones and the associated flow variability at fortnightly periods. Our study provides evidence for the temporal variation in buttressing forces and improves our understanding of the short-term response of ice-shelf flow to ocean tides. Our study suggests that in a warming climate, the long-term ice-flow speed will increase because ice-shelf thinning will reduce the resistive force arising from ephemeral grounding.

1 Introduction

The Antarctic Ice Sheet is fringed with floating ice shelves which have contact with sub-shelf bathymetric highs that generate resistive back stress to tributary ice flows (e.g., Thomas, 1979; Gudmundsson, 2013). This resistive stress, often referred to as buttressing stress, plays an important role in regulating Antarctic ice flows (e.g., Joughin et al., 2012; Pritchard et al., 2012). With ongoing and projected ice shelf thinning, the loss of buttressing stress will result in retreat, acceleration, and dynamic thinning of glaciers, and may eventually lead to catastrophic mass loss of the Antarctic Ice Sheet (e.g., Pritchard et al., 2009; Joughin et al., 2012; Alley et al., 2015). More detailed observation of the sub-shelf bathymetry, especially where ice shelves contact the seafloor, and better understanding of how the buttressing stress influences the ice-shelf-stream system are important for projecting the future evolution Antarctic ice sheet in response to changes in climate. Here, we focus on how the ocean tides influence the ice flow rate by modulating the buttressing stress.

Rutford Ice Stream (RIS), situated on the east of Ellsworth mountain range, is one of the major ice streams flowing into Filchner-Ronne Ice Shelf (FRIS) (Figure 1). RIS is about 300-km-long and 30-km-wide with a typical ice thickness of order 2 km over its grounded portion and 1.5 km over its floating portion. The bed of RIS lies more than 1.5 km below sea level and has a sinuous grounding line associated with a bathymetric ridge (Rignot et al., 2011b; King et al., 2016). The peak-to-peak tidal amplitude on the downstream ice shelf exceeds 7 m with the primary tidal constituents being semi-diurnal lunar and solar tides M_2 (12.42 h) and S_2(12.00 h), respectively (Table 1). The tidal forcing gives rise to a strong horizontal ice flow rate variation (∼20% of the mean flow speed) at the fortnightly period M_{sf} (14.77 day), which corresponds to the beating of the two primary semi-diurnal constituents M_2 and S_2 (e.g., Gudmundsson, 2006; Murray et al., 2007).

Using synthetic aperture radar (SAR) data collected by a 9-month COSMO-SkyMed (CSK) observation campaign over RIS, Minchew et al. (2017) inferred the spatial variability of the amplitude and phase of this fortnightly flow and found that it originated within the floating ice shelf and propagated upstream. This observation suggests that tidal forcing of the ice shelf processes is responsible for horizontal flow variability of the ice stream. Several models have been proposed to explain these observations including ephemeral grounding of the ice shelf, ice shelf margin widening, and grounding line migration (Minchew et al., 2017; Robel et al., 2017; Rosier & Gudmundsson, 2020; Warburton et al., 2020). All of these models suggest that the ocean tide modulates the contact of the ice shelf with the seafloor, and hence influences the buttressing stress to generate flow variability thereby causing temporal variability in flow.

Observation of the proposed tide-induced sub-shelf processes will improve our understanding of sub-shelf bathymetry and ice-shelf buttressing. Here, we focus on the tide-induced sub-shelf ephemeral grounding (Figure 2a). At RIS, there is a previously documented ephemeral grounding point 10 km downstream of the grounding line in the central trunk (Figure 1b, Goldstein et al., 1993; Rignot, 1998; Schmeltz et al., 2001). However, a modeling study on the buttressing effect of this single ephemeral grounding point, which is $\sim$1.5 m beneath the ice shelf central trunk, suggests that it has limited impact on modulating the ice flow (Schmeltz et al., 2001). More zones of ephemeral grounding which have not yet been documented may exist at RIS.

SAR images can be used to measure the displacement of ice over a given time interval in two orthogonal directions, one of which is purely horizontal along and parallel to the satellite orbit (azimuth) direction, and the other which is parallel to the radar line-of-sight (LOS) direction. The measurement in the LOS direction is sensitive to vertical motion. When SAR data has sufficiently high revisit rates and is collected from multiple viewing angles over the same point, one may infer the tide-induced time-dependent 3-D motions from a time series of displacements (Minchew et al., 2017). Minchew et al. (2017) parameterized the temporal behavior of the displacement as the sum of a small set of sinusoidal functions at known tidal periods and thus were by construction unable to observe any ephemeral grounding. In other words, ephemeral grounding produces temporal asymmetry that is not captured by such a simple parameterization.

Here, we develop new methods to map the ephemeral grounding zone and estimate the level of ephemeral grounding at RIS. We model the vertical displacements considering all relevant major tidal constituents and introduce the level of ephemeral grounding level, or so called clipping, as an additional parameter. We demonstrate and validate our methods using realistic synthetic tests and then apply the methods to an improved displacement dataset. We present the inferred displacement including maps of ephemeral grounding as well as updated estimates of the fortnightly flow variability at RIS.

2 SAR Data and Displacement Fields

As described in Minchew et al. (2017), the COSMO-SkyMed (CSK) SAR satellite constellation, which is operated by the Italian Space Agency (ASI), collected SAR data over RIS for approximately 9 months beginning in August 2013. The data acquisition plan covers all of the grounded ice and landward ∼100 km of the floating ice shelf from 32 unique tracks (Figure 1b). All four CSK satellites collected data, each repeating a given orbit track every 16 days. CSK satellite orbits are offset from one another with timespan between subsequent SAR acquisitions of 1, 3, 4, and 8 days. All CSK satellites carry nearly identical X-band (3.1 cm wavelength; 9.6 GHz) SAR systems. We use the Stripmap-HIMAGE products, which provide raw spatial resolution as fine as 3 m.

We processed the CSK data using the InSAR Scientific Computing Environment 2 (ISCE2) (Rosen et al., 2012). We first focused the raw images to single-look complex (SLC) images and then used the stack processing tools in ISCE2 (Fattahi et al., 2017) to coregister all the same-track SLC images using Antarctica digital elevation model BedMachine Version 2 (Morlighem et al., 2020). To calculate displacement fields from coregistered images, we prescribed the 2-D cross-correlation windows to be 480×240 pixels (range × azimuth) with a step size of 120 and 60 pixels in range and azimuth direction, respectively. The cross-correlation window takes into account that the ratio of the dimensions of a full resolution pixel is approximately 1:2. The cross-correlation window size is significantly larger than used in Minchew et al. (2017) (64×64 pixels). The use of a large cross-correlation window significantly increases the number of quality displacement measurements. We post-filter/adjust the resulting displacement fields by (1) masking out the displacement values if they differ from the prior Antarctica ice velocity model (Mouginot et al., 2012) beyond a prescribed threshold, (2) applying a moving-window median filter, and (3) adjusting for reference frame issue caused by miscoregistration using tie points on stagnant ice. This approach keeps as many valid measurements as possible from noisy displacement fields. Using this scheme, we derived ∼2500 displacement fields along 32 tracks using pairs with no greater than 8-day intervals.

Using dense cross-correlation on the SLC images to estimate displacement fields is computationally expensive, especially when using large cross-correlation windows. To reduce computation time, we have developed a new tool employing GPUs for estimating the displacement fields. This GPU-enabled software accelerates this expensive computation by factors of 10 to 100 and makes it viable to use large cross-correlation windows, such as 480×240 pixels. This new tool has been included as part of the publicly released version of ISCE2 (Zhu et al., 2022).

3 Methodology

3.1 Ocean tides, Bathymetry and Ephemeral Grounding

Ocean tides cause changes in instantaneous sea level from the mean sea level. By convention, positive tide height corresponds to a rise in sea level, and zero tide height corresponds to mean sea level. Ice shelves rise and fall synchronously with ocean tide. At any point on an ice shelf, the sub-shelf water column thickness (WCT) is the distance between the underlying seafloor and the bottom of ice shelf when tide height is zero. Ephemeral grounding occurs when the impact of tide on the instantaneous level of the bottom of ice shelf exceeds WCT such that the bottom of ice shelf contacts the seafloor. Figures 2a1 and 2a2 is an example of ephemeral grounding on a sub-shelf bathymetric pinning point where the WCT is 1 m.

At any point, the vertical displacement at the surface of ice shelf is the same as the vertical displacement of the bottom of the ice shelf (assuming negligible vertical strain), if we define the zero displacement for both to be the their levels when tide height is zero, respectively. Hereafter, unless mentioned explicitly, vertical displacement refers to displacement at surface which SAR observations have direct sensitivity to. The vertical displacement is typically the same as the tide height due to hydrostatic balance between ice shelf and ocean (Figure 2a1), for example, in the central trunk of the ice shelf. In the vicinity of the grounding zone, the amplitude of surface vertical displacement gradually decreases to zero towards the grounded ice due to the flexure of the ice shelf (e.g., Vaughan, 1995).

Ephemeral grounding on sub-shelf bathymetric highs induces clipping on the vertical displacement. We define the level of ephemeral grounding as the level of clipping (Figure 2b1). In the example shown in Figure 2, the vertical displacement at the point indicated by the gray GPS station is clipped at -1 m because the seafloor is 1 m below the mean level of the bottom of ice shelf. The level of ephemeral grounding is typically negative and is equivalent to be negative of the WCT. A higher level of grounding corresponds to higher sub-shelf bathymetry and thinner WCT, and vice versa. If the range of vertical displacement is smaller than the WCT, ephemeral grounding does not occur. We note the difference between grounding zone and zones of ephemeral grounding. Grounding zone refers to the transition region between the fully grounded ice to the free floating ice shelf (e.g., Fricker et al., 2009). While zones of ephemeral grounding are likely to exist in the vicinity of the grounding zone due to the shallow bathymetry, they can also exist far from the grounding zone, for example, an isolated localized bathymetric high point in the central trunk of the ice shelf.

3.2 An Overview of Displacement Models and Workflow

Our approach includes two displacement models: a linear 3-D displacement model for indirectly inferring ephemeral grounding and a nonlinear 3-D displacement model for quantifying the level of ephemeral grounding. The workflow starts from the linear model, then constructs the nonlinear model using the results derived from the linear model and an independent ocean tidal model, and finally solves for vertical displacements with ephemeral grounding and horizontal flow variability (Figure 3).

The linear model uses the same framework as the model developed in Minchew et al. (2017), but is modified to improve the estimation of the vertical displacements on the ice shelf and to identify zones of ephemeral grounding. A key improvement is the inclusion of the vertical displacement at fortnightly period into the inference. In section 3.3, we show the connection between ephemeral grounding and the inferred vertical displacement at fortnightly period. The main limitation of the linear model is that only a subset of tidal periods can be inferred (e.g., M_2, O_1), in particular, those which are not aliased in the satellite observations, which occur at the same time of a day. As a consequence, this linear model is unable to constrain the level of ephemeral grounding (Figure 2a) which depends on knowledge of the total displacement field, not just selected tidal constituents.

To quantify the level of ephemeral grounding, the displacement model needs to consider the absolute vertical displacement on the ice shelf, which is the superposition of vertical displacement at all tidal periods (Table 1). Our strategy is to combine inferred vertical displacements derived from the linear model and the vertical displacements extracted from the ocean tidal model. The former has high spatial resolution but misses key aliased tidal constituents. The latter is complete including all major tidal constituents but does not have sufficient spatial resolution for resolving ephemeral grounding (e.g., in the vicinity of the grounding zone) due to the lack of knowledge of the bathymetry beneath ice shelves. By combination of the two, we construct a nonlinear vertical displacement model accounting for ephemeral grounding.

The full workflow consists of two parts which include two models and four steps (Figure 3). Part I is associated with the linear 3-D displacement model. We apply this model to real data and infer vertical displacements at the selected tidal periods (Step 1). Then, we obtain the theoretical bias in the estimated vertical displacements from a realistic synthetic test and correct for this bias in the inferred values (Step 2). Part II describes the nonlinear 3-D displacement model. We construct the nonlinear vertical displacement model accounting for ephemeral grounding using the bias-corrected inferred vertical displacements from the linear model and the ocean tidal model (Step 3). Using this new vertical displacement model and inheriting the horizontal displacement model from the linear 3-D displacement model, we arrive at the final nonlinear 3-D displacement model. Using this model, we infer the vertical displacements with ephemeral grounding and horizontal flow variability (Step 4).

3.3 Identifying Zones of Ephemeral Grounding

3.3.1 A Linear Model for Inferring 3-D Periodic Displacements

We start with reviewing the methodology developed in Minchew et al. (2017) which forms the basic foundation for our methodological development. In this review, we include our modification to the original inverse problem formulation which makes the model more suitable for our use. We are interested in the tide-induced displacements of ice stream and ice shelf system. We consider the instantaneous 3-D displacement vector $\mathbf{u}$ on the ice surface at location $\mathbf{r}$ and at time t as the sum of a secular term and a tide-induced term in east ($\hat{e}$), north ($\hat{n}$), and up component ($\hat{u}$), such that

$$\mathbf{u}(\mathbf{r},t) = \mathbf{v}(\mathbf{r})t + \mathbf{w}(\mathbf{r},t) = \begin{bmatrix} v^{\hat{e}}(\mathbf{r}) \\ v^{\hat{n}}(\mathbf{r}) \\ v^{\hat{u}}(\mathbf{r}) \end{bmatrix} t + \begin{bmatrix} w^{\hat{e}}(\mathbf{r},t) \\ w^{\hat{n}}(\mathbf{r},t) \\ w^{\hat{u}}(\mathbf{r},t) \end{bmatrix} \tag{1}$$

where $\mathbf{v}(\mathbf{r})$ is the secular velocity and $\mathbf{w}(\mathbf{r},t)$ is the tide-induced displacement vector.

Assuming the tide-induced displacement to be sinusoidal for all periods of tidal forcing, we parameterize $\mathbf{w}(\mathbf{r},t)$ as the sum of a family of sinusoidal functions $i = 1, 2, ..., k$, such that

$$w^{\hat{\zeta}}(\mathbf{r},t) = \sum_{i=1}^{k} a_i^{\hat{\zeta}} \sin(\omega_i t + \phi_i^{\hat{\zeta}}) \quad \text{for } \hat{\zeta} = [\hat{e}, \hat{n}, \hat{u}] \tag{2}$$

where sinusoid i has angular frequency ω_i, amplitude $a_i^{\hat{\zeta}}(\mathbf{r})$, and phase $\phi_i^{\hat{\zeta}}(\mathbf{r})$ corresponding to different tidal constituents. We can rewrite equation (2) as the linear displacement model

$$w^{\hat{\zeta}}(\mathbf{r},t) = \sum_{i=1}^{k} c_i^{\hat{\zeta}} \cos(\omega_i t) + s_i^{\hat{\zeta}} \sin(\omega_i t) \tag{3}$$

where

$$c_i^{\hat{\zeta}} = a_i^{\hat{\zeta}} \sin(\phi_i^{\hat{\zeta}}) \tag{4}$$

$$s_i^{\hat{\zeta}} = a_i^{\hat{\zeta}} \cos(\phi_i^{\hat{\zeta}}). \tag{5}$$

At any point $\mathbf{r}$, the measured displacement $d_j (j = 1, 2, \cdots, q)$ from q pairs of SAR scenes is

$$d_j(\hat{\mathbf{l}}_j, \mathbf{r}, t_j^a, t_j^b) = \hat{\mathbf{l}}_j \cdot (\mathbf{u}(\mathbf{r}, t_j^b)) - \mathbf{u}(\mathbf{r}, t_j^a)) \tag{6}$$

where $\hat{\mathbf{l}}_j$ is observational unit vector (in LOS or azimuth direction) and t_j^a and t_j^b are the acquisition times of the primary and secondary scenes of the SAR pair.

Equation (6) relates model parameters ($\mathbf{v}$, $c_i^{\hat{\zeta}}$, $s_i^{\hat{\zeta}}$) to the observed displacements. To infer the model parameters, we cast it as a linear inverse problem for a given location $\mathbf{r}$ and arrive at the matrix form

$$\mathbf{d} = \mathbf{G}\mathbf{m} \tag{7}$$

where $\mathbf{d}$ is the vector of observed displacement, $\mathbf{m}$ is the model vector, and $\mathbf{G}$ is the design matrix. Model vector $\mathbf{m}$ has the form

$$\mathbf{m} = \begin{bmatrix} \mathbf{v} & \mathbf{c}_1 & \mathbf{s}_1 & \mathbf{c}_2 & \mathbf{s}_2 & ... & \mathbf{c}_k & \mathbf{s}_k \end{bmatrix}^T \tag{8}$$

$$\mathbf{c}_i = \begin{bmatrix} c_i^{\hat{e}} & c_i^{\hat{n}} & c_i^{\hat{u}} \end{bmatrix}, i = 1, 2, .., k \tag{9}$$

$$\mathbf{s}_i = \begin{bmatrix} s_i^{\hat{e}} & s_i^{\hat{n}} & s_i^{\hat{u}} \end{bmatrix}, i = 1, 2, .., k \tag{10}$$

and the corresponding design matrix has the form

$$\mathbf{G} = \begin{bmatrix} \hat{\mathbf{l}}_1 \Delta t_1 & \hat{\mathbf{l}}_1 \Delta p_{1_1}^{\cos} & \hat{\mathbf{l}}_1 \Delta p_{1_1}^{\sin} & \dots & \hat{\mathbf{l}}_1 \Delta p_{k_1}^{\cos} & \hat{\mathbf{l}}_1 \Delta p_{k_1}^{\sin} \\ \vdots & & & \ddots & & \vdots \\ \hat{\mathbf{l}}_q \Delta t_q & \hat{\mathbf{l}}_q \Delta p_{1_q}^{\cos} & \hat{\mathbf{l}}_q \Delta p_{1_q}^{\sin} & \dots & \hat{\mathbf{l}}_q \Delta p_{k_q}^{\cos} & \hat{\mathbf{l}}_q \Delta p_{k_q}^{\sin} \end{bmatrix} \tag{11}$$

where

$$\Delta t_j = t_j^b - t_j^a \tag{12}$$

$$\Delta p_{i_j}^{\cos} = \cos(\omega_i t_j^b) - \cos(\omega_i t_j^a) \tag{13}$$

$$\Delta p_{i_j}^{\sin} = \sin(\omega_i t_j^b) - \sin(\omega_i t_j^a). \tag{14}$$

To solve the inverse problem, we adopt Bayesian formulation assuming Gaussian distributions for all uncertainties, so the optimal (maximum a posteriori) model estimation is (e.g., Tarantola, 2005)

$$\tilde{\mathbf{m}} = (\mathbf{G}^T \mathbf{C}_\chi^{-1} \mathbf{G} + \mathbf{C}_m^{-1})^{-1} (\mathbf{C}_\chi^{-1} \mathbf{G}^T \mathbf{d} + \mathbf{C}_m^{-1} \mathbf{m}_0) \tag{15}$$

where $\mathbf{m}_0$ is the prior model vector, $\mathbf{C}_m$ is the prior model covariance matrix, and $\mathbf{C}_\chi$ is the error covariance matrix, also referred to as the misfit covariance. In the original formulation, the error covariance matrix is denoted as $\mathbf{C}_d$, because only the measurement error in data is considered. Here, we consider both measurement error and modeling (or prediction) error, $\mathbf{C}_p$, such that $\mathbf{C}_\chi = \mathbf{C}_d + \mathbf{C}_p$. Details of $\mathbf{C}_\chi$ are discussed in section 3.5.

We design $\mathbf{C}_m$ to be diagonal and structured as follows:

$$\mathbf{C}_m^{-1} = \mathrm{diag}[\Omega_{\mathbf{v}}\ \Omega_{\mathbf{c}_1}\ \Omega_{\mathbf{s}_1}\ \cdots\ \Omega_{\mathbf{c}_k}\ \Omega_{\mathbf{s}_k}\ ] \tag{16}$$

$$\Omega_{\mathbf{v}} = [\Omega_{\mathbf{v}^{\hat{\mathbf{e}}}}\ \Omega_{\mathbf{v}^{\hat{\mathbf{n}}}}\ \Omega_{\mathbf{v}^{\hat{\mathbf{u}}}}\ ] \tag{17}$$

$$\Omega_{\mathbf{c}_i} = [\Omega_{c_i^{\hat{e}}}\ \Omega_{c_i^{\hat{n}}}\ \Omega_{c_i^{\hat{u}}}], \tag{18}$$

$$\Omega_{\mathbf{s}_i} = [\Omega_{s_i^{\hat{e}}}\ \Omega_{s_i^{\hat{n}}}\ \Omega_{s_i^{\hat{u}}}] \tag{19}$$

$$\Omega_\rho = \begin{cases} \frac{1}{\epsilon^2} & \rho \text{ is constrained to be close to the prior value} \\ 0 & \rho \text{ is unconstrained} \end{cases} \quad (\rho = v^{\hat{\xi}},\ c_i^{\hat{\xi}},\ s_i^{\hat{\xi}}) \tag{20}$$

where ϵ is a pre-defined value of small variation in parameters. Constraining the variations of certain components to be small helps stabilize the inversion when the unconstrained inversion shows strong trade-offs between certain components (Minchew et al., 2017).

In the original design of the model prior, $\mathbf{C}_m$ is a diagonal matrix with the diagonal values constraining the amplitude of the corresponding variation. Two reference frequencies were chosen for the horizontal and vertical variation, respectively, and diagonal values scaled inversely with the difference between the corresponding frequency and the reference frequency. This approach was motivated by the fact the vertical and horizontal motion at RIS are primarily at short-period (semi-diurnal and diurnal) and at long-period (fortnightly), respectively. Here, we remove the dependence on reference frequency and generalize the model so that both the short-period and long-period variation can be modeled.

The posterior model covariance matrix

$$\tilde{\mathbf{C}}_m = (\mathbf{G}^T \mathbf{C}_\chi^{-1} \mathbf{G} + \mathbf{C}_m^{-1})^{-1} \tag{21}$$

provides the estimates of formal errors in $\tilde{\mathbf{m}}$. The estimates of formal errors in amplitude $a_i^{\hat{\zeta}}$ and phase $\phi_i^{\hat{\zeta}}$ can be calculated from the formal errors of $c_i^{\hat{\zeta}}$ and $s_i^{\hat{\zeta}}$ by applying the following relations derived in Minchew et al. (2017):

$$\sigma^2_{a_i^{\hat{\zeta}}} = \frac{\sigma^2_{c_i^{\hat{\zeta}}} \sin^2(\phi_i^{\hat{\zeta}}) - \sigma^2_{s_i^{\hat{\zeta}}} \cos^2(\phi_i^{\hat{\zeta}})}{\sin^4(\phi_i^{\hat{\zeta}}) - \cos^4(\phi_i^{\hat{\zeta}})} \tag{22}$$

$$\sigma^2_{\phi_i^{\hat{\zeta}}} = \frac{-\sigma^2_{c_i^{\hat{\zeta}}} \cos^2(\phi_i^{\hat{\zeta}}) + \sigma^2_{s_i^{\hat{\zeta}}} \sin^2(\phi_i^{\hat{\zeta}})}{(a_i^{\hat{\zeta}})^2(\sin^4(\phi_i^{\hat{\zeta}}) - \cos^4(\phi_i^{\hat{\zeta}}))} \tag{23}$$

3.3.2 An Approach to Infer the Presence of Ephemeral Grounding

3.3.2.1 Candidate Tidal Constituents

We choose the family of sinusoids in the model according to our prior knowledge of the tide-induced displacement variations at RIS. The vertical motion on the ice shelf is dominated by semi-diurnal and diurnal constituents (Table 1). However, the time interval of the SAR acquisitions is always within seconds of being integer days, which prevents any sensitivity to constituents S_2, K_2, K_1, and P_1 whose periods are or very close to 12 h or 24 h. Thus, we are left with M_2(12.42 h period), N_2(12.66 h period), O_1(25.82 h period), and Q_1(26.87 h period).

3.3.2.2 Ephemeral Grounding and the Vertical M_{sf} Sinusoid

When the ice shelf ephemerally grounds on the seafloor (Figure 2a), the vertical displacement is the time series of the tide height clipped at the grounding level (Figure 2b1-2b2). Compared with the original time series, such clipping introduces power at fortnightly periods, as can be seen in the amplitude spectrum (Figure 2b3- 2b4). Therefore, we include the vertical M_{sf} period into the model and consider it as a proxy for detecting ephemeral grounding. If the inferred amplitude of the vertical M_{sf} sinusoid is significantly larger than the expected amplitude (less than 1 cm at RIS), the vertical displacement can be assumed to be ephemerally grounded. Later, in section 3.4, we will explicitly include the clipping effect in the model parameterization, but doing so renders the model nonlinear.

3.3.3 Tests with Synthetic Data

We use synthetic tests to explore how to best identify ephemeral grounding and to assess any bias in the linear approach. Within the context of linear model, we construct our synthetic model as follows:

1. Secular velocity: We prescribe the east and north components of the secular velocity, $v^{\hat{e}}$, and, $v^{\hat{n}}$, using the latest Antarctic Ice Velocity Model (Rignot et al., 2011b; Mouginot et al., 2012). We prescribe the up component, $v^{\hat{u}}$, to be zero everywhere.

2. Vertical tidal displacement: We prescribe the vertical motion on the ice shelf with ephemeral grounding as:

$$w^{\hat{u}}(\mathbf{r}, t) = \max(S(\mathbf{r})h_{\text{ref}}(t), K(\mathbf{r})) \tag{24}$$

   where $h_{\text{ref}}(t)$ is tide height time series extracted at a reference point in the ice shelf trunk (Figure 1b) from the CATS2008 ocean tidal model (Padman et al., 2002), $S(\mathbf{r})$ is a linear amplitude scaling factor, and $K(\mathbf{r})$ is the level of ephemeral grounding. $S(\mathbf{r})$ is 1 in the ice shelf central trunk, gradually decreasing in the vicinity of the grounding zone and is 0 over the grounded ice. We adopt this parameterized form using a reference point because the tidal model does not have data available everywhere in our observational domain and it does not have sufficient resolution near grounding zones. This form for the synthetic model assumes negligible variation in phase over the ice shelf, a reasonable approximation according to both the tidal model and our eventual inferred values from real data.

3. Horizontal tidal displacements: We prescribe the temporal variation in horizontal flow rate, $\Delta\mathbf{v}^{\text{horiz}}(\mathbf{r}, t)$, to be only in the same direction as the secular velocity ("along-flow") and to scale with the horizontal secular speed as

$$\begin{aligned}\Delta\mathbf{v}^{\text{horiz}}(\mathbf{r}, t) &= [\Delta v^{\hat{e}}(\mathbf{r}, t), \Delta v^{\hat{n}}(\mathbf{r}, t)] \\ &= \begin{cases} (v^{\text{horiz}}(\mathbf{r})/v_0) \sum_{\xi} a_{\xi} \sin(\omega_{\xi} t + \phi_{\xi}) & \text{along-flow} \\ 0 & \text{cross-flow} \end{cases}\end{aligned} \tag{25}$$

where the a_ξ and ϕ_ξ are the reported amplitude and phase of the flow rate variation at the period of tidal constituent ξ by GPS measurements at RIS (Murray et al., 2007), $v^{\text{horiz}}(\mathbf{r}) = \sqrt{v^{\hat{e}^2}(\mathbf{r}) + v^{\hat{n}^2}(\mathbf{r})}$ is the prescribed horizontal secular speed, and v_0 is the reference horizontal secular speed in the central trunk of RIS, which we choose to be $1\,\text{m/d}$.

4. Synthetic displacement data: We create synthetic displacements which have the same temporal and spatial sampling as our actual observations (see section 2). We add uncorrelated Gaussian noise with standard deviation 10 cm to both the LOS and azimuth synthetic displacements.

We conduct synthetic tests exploring models with different families of sinusoids, different settings of model priors, and both sub-shelf grounding and no-grounding scenarios. In the no-grounding case, $K(\mathbf{r})$ is prescribed as lower than lowest tide height (e.g., $-0.5\,\text{m}$). In the ephemeral grounding case, we prescribe $K(\mathbf{r})$ to $-1.5\,\text{m}$ everywhere. We conclude that the optimal model contains sinusoids M_2, N_2, O_1, and M_{sf}, adopts a prior model with $\mathbf{m}_0 = 0$, and prior model covariance matrix constraining the horizontal variations at short periods (M_2, N_2, O_1) to be small ($\epsilon = 1\,\text{mm}$ in equation 20). The result and discussion of synthetic tests are provided in the supporting information Text S1. These demonstrate that the inferred amplitude of vertical M_{sf} can be used as a proxy for detecting, but not quantifying ephemeral grounding. By comparing the inferred values with the prescribed values, the synthetic tests also provide estimates of the bias in the inferred values. The bias estimates are important for interpreting and using the results inferred with real data.

3.4 Quantifying of Level of Ephemeral Grounding

3.4.1 A Vertical Displacement Model with Ephemeral Grounding

In order to identify zones of ephemeral grounding, as well as to constrain the level of ephemeral grounding, we need to develop a new vertical displacement model for $w^{\hat{u}}(\mathbf{r}, t)$ in equation (1). Compared with the linear model, the new model needs to consider the absolute ocean tide height i.e., the superposition of all major constituents (Table 1). However, as previously noted, we are not able to directly infer a few major constituents (e.g., S_2, K_1) with periods at or close to 12h and 24h, since they are aliased in the CSK observations. (Repeating periods of CSK observations are integer multiples of 24 h.) To overcome this limitation, we refer to the existing ocean tidal models which can provide a starting point from which we can infer the aliased constituents. The ocean tidal models provide the tie between the constituents we can observe and those we cannot. The major limitation of tidal models at RIS is that they do not have sufficient spatial resolution in the vicinity of the grounding zone where we expect amplitudes to gradually decrease towards the grounded ice due to ice-shelf flexure as well as possible variations in phase as observed in Minchew et al. (2017).

The new vertical displacement model we develop combines the completeness of the ocean tidal model with the high spatial resolution of inferred displacement variation at M_2, N_2, and O_1 periods from our CSK data using the linear model (section 3.3). We use the CATS2008 tidal model (Padman et al., 2002), which is shown to agree well with local GPS measurements (Padman et al., 2018). We separately construct the spatial phase and amplitude maps for the 10 major tidal constituents listed in Table 1 over the ice shelf, from which we have the absolute tidal displacement. Then, we introduce ephemeral grounding level as an additional parameter which clips the absolute tidal displacement to arrive at our final vertical displacement model. We present this model in three parts as follows:

1. Spatial phase variation

   We denote the spatial phase variation for a given constituent ξ, as $\phi_\xi(\mathbf{r})$ and define its relative spatial phase variations as:

$$\Delta\phi_\xi(\mathbf{r}) = \phi_\xi(\mathbf{r}) - \phi_\xi(\mathbf{r}_0) \tag{26}$$

   where $\mathbf{r}_0$ is a chosen reference point in the central trunk of the ice shelf (Figure 1b). Using the inferred spatial phase variation of M_2, N_2, and O_1 from the linear model, we have an estimate of the relative spatial phase variation, which we denote as $\Delta\tilde{\phi}_{M_2}(\mathbf{r})$, $\Delta\tilde{\phi}_{N_2}(\mathbf{r})$, and $\Delta\tilde{\phi}_{O_1}(\mathbf{r})$, where the tilde symbol on top signifies an estimated value. We assume that constituents with similar periods have a similar physical response, so that they share the same relative phase variation. This assumption leads us to the following assumptions on the other 5 semi-diurnal and diurnal constituents:

$$\begin{aligned} &\Delta\tilde{\phi}^{\hat{u}}_{S_2}(\mathbf{r}) = \Delta\tilde{\phi}^{\hat{u}}_{K_2}(\mathbf{r}) = \Delta\tilde{\phi}^{\hat{u}}_{M_2}(\mathbf{r}) \\ &\Delta\tilde{\phi}^{\hat{u}}_{K_1}(\mathbf{r}) = \Delta\tilde{\phi}^{\hat{u}}_{P_1}(\mathbf{r}) = \Delta\tilde{\phi}^{\hat{u}}_{Q_1}(\mathbf{r}) = \Delta\tilde{\phi}^{\hat{u}}_{O_1}(\mathbf{r}) \end{aligned}. \tag{27}$$

   Our choice of pairing S_2 and K_2 with M_2 is because the phase of M_2 is better constrained than N_2 due to its larger amplitude. As will be shown when using the actual data, $\Delta\tilde{\phi}_{M_2}(\mathbf{r})$ and $\Delta\tilde{\phi}_{N_2}(\mathbf{r})$ are similar. The linear inversion does not provide access to the phase of M_f and M_m. Because their amplitudes are significantly smaller than other constituents (Table 1), there is little impact if we ignore their phase variations.

We estimate the spatial variations in phase for all tidal constituents by combining the phase at the reference point with the estimated relative phase variation:

$$\phi_\xi(\mathbf{r}) = \phi_\xi(\mathbf{r}_0) + \Delta\tilde{\phi}_\xi(\mathbf{r}) \tag{28}$$

where $\phi_\xi(\mathbf{r}_0)$ is the phase of constituent ξ at the reference point and is set by the value extracted from the tide model.

2. Spatial amplitude variation

The inferred amplitude maps in both Minchew et al. (2017) and our new results (section 4.1) suggest that the spatial variations of amplitude in the vicinity of the grounding zone due to ice-shelf flexure are very similar for M_2, N_2, O_1. Therefore, we empirically assume the same normalized spatial amplitude variation for all tidal periods and adopt the following form for the spatial amplitude variation:

$$a_\xi(\mathbf{r}) = A(\mathbf{r})a_\xi(\mathbf{r}_0). \tag{29}$$

Here, $a_\xi(\mathbf{r}_0)$ is the amplitude of constituent ξ at the reference point and is set by the value from the tide model. $A(\mathbf{r})$, a new parameter, is the linear scaling of the amplitude at $\mathbf{r}$ to account for the decreasing amplitude in the vicinity of the grounding zone. We present a more detailed discussion on using $A(\mathbf{r})$ in the supporting information Text S6.

3. Ephemeral grounding level

A new parameter, $K(\mathbf{r})$, denotes the ephemeral grounding level (section 3.1 and Figure 2b). Given the formulated spatial variations of the phase and the amplitude for all constituents, we arrive at the final vertical displacement model including ephemeral grounding:

$$w^{\hat{u}}(\mathbf{r},t) = \max\Big(\sum_\xi A(\mathbf{r})a_\xi(\mathbf{r}_0)\sin(\omega_\xi t + \phi_\xi(\mathbf{r})), K(\mathbf{r})\Big) \tag{30}$$

where $a_\xi(\mathbf{r})$ and $\phi_\xi(\mathbf{r})$ are given by equations (28) and (29). The parameters characterizing the vertical displacement are $A(\mathbf{r})$ and $K(\mathbf{r})$. The inclusion of $K(\mathbf{r})$ causes this new displacement model to be nonlinear.

3.4.2 Model for Inferring Ephemeral Grounding Level

Applying the new vertical displacement model to the vertical component of tide-induced displacement (equation 2), we arrive at the new model for simultaneously inferring the 3-D surface displacement variation with ephemeral grounding level explicitly taken into account. At any point $\mathbf{r}$, given q displacement observations d_j ($j = 1, 2, \cdots, q$) with the corresponding observational unit vector $\hat{\mathbf{l}}_j$, and the acquisition time of primary scene t_j^a and secondary scene t_j^b, we denote this nonlinear model as

$$\mathbf{d} = \mathbf{g}(\mathbf{v}, \mathbf{m}^{\hat{e}}, \mathbf{m}^{\hat{n}}, A, K) \tag{31}$$

where $\mathbf{d}$ is the vector of observed displacement, $\mathbf{g}$ represents the forward function relating the model parameters to the observations, and the model parameters consist of secular velocity $\mathbf{v} = \begin{bmatrix} v^{\hat{e}} & v^{\hat{n}} & v^{\hat{u}} \end{bmatrix}^T$, parameters for the tide-induced sinusoidal horizontal displacement variation in east and north component $\mathbf{m}^{\hat{e}} = \begin{bmatrix} c_1^{\hat{e}} & s_1^{\hat{e}} & \ldots & c_k^{\hat{e}} & s_k^{\hat{e}} \end{bmatrix}^T$, $\mathbf{m}^{\hat{n}} = \begin{bmatrix} c_1^{\hat{n}} & s_1^{\hat{n}} & \ldots & c_k^{\hat{n}} & s_k^{\hat{n}} \end{bmatrix}^T$, and the amplitude scaling A and ephemeral grounding level K for the vertical displacement. Given the point $\mathbf{r}$, the forward function $\mathbf{g}(\mathbf{m})$ is formulated as follows:

The observed displacement d_j is the 3-D displacement over $[t_j^a, t_j^b]$ projected onto $\hat{\mathbf{l}}_j$, such that

$$\mathbf{d} = \mathbf{g}(\mathbf{v}, \mathbf{m}^{\hat{e}}, \mathbf{m}^{\hat{n}}, A, K) = \begin{bmatrix} \hat{\mathbf{l}}_1^T \cdot \Delta\mathbf{u}_1 \\ \hat{\mathbf{l}}_2^T \cdot \Delta\mathbf{u}_2 \\ \vdots \\ \hat{\mathbf{l}}_q^T \cdot \Delta\mathbf{u}_q \end{bmatrix} \tag{32}$$

where $\Delta\mathbf{u}_j$ is the 3-D displacement vector over the corresponding time interval. We stack the transpose of these vectors by row and form a matrix

$$\begin{bmatrix} \Delta\mathbf{u}_1^T \\ \Delta\mathbf{u}_2^T \\ \vdots \\ \Delta\mathbf{u}_q^T \end{bmatrix} = \begin{bmatrix} \Delta u_1^{\hat{e}} & \Delta u_1^{\hat{n}} & \Delta u_1^{\hat{u}} \\ \Delta u_2^{\hat{e}} & \Delta u_2^{\hat{n}} & \Delta u_2^{\hat{u}} \\ \vdots & \vdots & \vdots \\ \Delta u_q^{\hat{e}} & \Delta u_q^{\hat{n}} & \Delta u_q^{\hat{u}} \end{bmatrix} \tag{33}$$

where the three columns are the east, north, and up component of the displacement vectors.

For the east and north component, the relationship with parameters is linear:

$$\begin{bmatrix}\Delta u_1^{\hat{\eta}}\\ \Delta u_2^{\hat{\eta}}\\ \vdots\\ \Delta u_q^{\hat{\eta}}\end{bmatrix} = \begin{bmatrix}u^{\hat{\eta}}(t_1^b)-u^{\hat{\eta}}(t_1^a)\\ u^{\hat{\eta}}(t_2^b)-u^{\hat{\eta}}(t_2^a)\\ \vdots\\ u^{\hat{\eta}}(t_q^b)-u^{\hat{\eta}}(t_q^a)\end{bmatrix} = \begin{bmatrix}\Delta t_1\\ \Delta t_2\\ \vdots\\ \Delta t_q\end{bmatrix} v^{\hat{\eta}} + \begin{bmatrix}\Delta t_1 & \Delta p_{1_1}^{\cos} & \Delta p_{1_1}^{\sin} & \dots & \Delta p_{k_1}^{\cos} & \Delta p_{k_1}^{\sin}\\ \vdots & & & \ddots & & \vdots\\ \Delta t_q & \Delta p_{1_q}^{\cos} & \Delta p_{1_q}^{\sin} & \dots & \Delta p_{k_q}^{\cos} & \Delta p_{k_q}^{\sin}\end{bmatrix}\mathbf{m}^{\hat{\eta}} \tag{34}$$

where $\hat{\eta} = [\hat{e}, \hat{n}]$, $\mathbf{m}^{\hat{\eta}}$ is the corresponding model parameter vector, Δt_j, $\Delta p_{i_j}^{\cos}$, $\Delta p_{i_j}^{\sin}$ $(i = 1, 2, .., k,\ j = 1, 2, ..., q)$ are defined in equation (12) to (14).

For the up component, the secular term remains the same, but the tide-induced term is set by the new nonlinear vertical displacement model:

$$\begin{bmatrix}\Delta u_1^{\hat{u}}\\ \Delta u_2^{\hat{u}}\\ \vdots\\ \Delta u_q^{\hat{u}}\end{bmatrix} = \begin{bmatrix}\Delta t_1\\ \Delta t_2\\ \vdots\\ \Delta t_q\end{bmatrix} v^{\hat{u}} + \begin{bmatrix}w^{\hat{u}}(t_1^b)-w^{\hat{u}}(t_1^a)\\ w^{\hat{u}}(t_2^b)-w^{\hat{u}}(t_2^a)\\ \vdots\\ w^{\hat{u}}(t_q^b)-w^{\hat{u}}(t_q^a)\end{bmatrix} \tag{35}$$

where $w^{\hat{u}}(t)$, a function of A and K, is defined in equation (30).

3.4.3 A Necessary Condition for Constraining Ephemeral Grounding Level

Ephemeral grounding occurs at lower tides when the total low tide height exceeds the sub-shelf water column thickness. To constrain the ephemeral grounding level, we need satellite data acquired during the period of grounding. Considering that SAR data is temporally sparse (i.e., time interval of a few days), it is possible that little or no data is acquired during periods of ephemeral grounding, especially when the grounding level is low. For any location, a necessary condition for constraining the level of ephemeral grounding is that at least one SAR scene is acquired during ephemeral grounding.

This necessary condition is also reflected in the formulation of the displacement model. Equation (35) indicates that the vertical displacement model is constructed by discrete vertical displacement values at the acquisition times of the SAR scenes $w^{\hat{u}}(t)$, where $t = t_1^a, t_1^b, t_2^a, t_2^b, \cdots, t_q^a, t_q^b$. At any location $\mathbf{r}$, according to equation (30), for the ephemeral grounding level K_{true} to take effect in constructing the model, we need to assume that

$$\text{There exists } t^* \text{ in } \{t_1^a, t_1^b, t_2^a, t_2^b, \cdots, t_q^a, t_q^b\} \quad \text{such that} \quad K_{\text{true}} > \sum_{\xi} Aa_{\xi}\sin(\omega_{\xi}t^* + \phi_{\xi}). \tag{36}$$

Equation (36) implies that the lowest ephemeral grounding level that the data can constrain in theory is

$$K_{\min} = \min(\sum_{\xi} Aa_{\xi}^{\hat{u}} \sin(\omega_{\xi} t^* + \phi_{\xi}^{\hat{u}}) \quad | \quad t^* \in \{t_1^a, t_1^b, t_2^a, t_2^b, \cdots, t_q^a, t_q^b\}) \tag{37}$$

and the necessary condition to constrain ephemeral grounding level K_{true} is

$$K_{\text{true}} > K_{\min}. \tag{38}$$

At locations, where the vertical displacement without clipping is the same as tide height (e.g., the central trunk of ice shelf), $A = 1$ in equation (36), and the necessary condition can be described as the level of ephemeral grounding being higher than the minimum of all sampled tide heights. At locations, where the vertical displacement is damped to be smaller than the tide height (e.g., the vicinity of the grounding zone), we can still use the sampled tide heights at this location to assess the ability of SAR data in detecting ephemeral grounding, because a lower sampled tide height always corresponds to a lower sampled level of vertical displacement, unless already being clipped at a higher level.

If the ephemeral grounding level cannot be constrained, there are two possibilities: (1) there is no ephemeral grounding, or (2) there is ephemeral grounding, but the grounding level K_{true} is so low that the necessary condition is not satisfied. The second possibility implies that any region of ephemeral grounding zone we infer is a lower bound on the actual extent of ephemeral grounding. In section 5.3, we present further discussion on the implication of this necessary condition.

3.4.4 Formulating and Solving the Inverse Problem

We adopt a Bayesian formulation of the inverse problem assuming Gaussian distributions for all uncertainties. The posterior probability distribution of the model parameters is (Tarantola, 2005):

$$P(\mathbf{m}|\mathbf{d}) \propto P(\mathbf{d}|\mathbf{m})P(\mathbf{m}) \tag{39}$$

$$P(\mathbf{d}|\mathbf{m}) \propto \exp(-\frac{1}{2}(\mathbf{d} - \mathbf{g}(\mathbf{m}))^T \mathbf{C}_{\chi}^{-1}(\mathbf{d} - \mathbf{g}(\mathbf{m}))) \tag{40}$$

where $P(\mathbf{m})$ is model prior, $P(\mathbf{d}|\mathbf{m})$ is the data likelihood, and $\mathbf{C}_{\chi}$ is the error covariance matrix discussed in section 3.5. The model prior for secular velocity and horizontal displacement variations is the same as those in the linear model. We adopt a uniform prior for amplitude scaling A in the range of $[0, 2]$ and a uniform prior for the ephemeral grounding K in the range of minimal and maximal tide height at RIS.

We consider each location to be independent of other locations. The total number of grid points are $10^5 \sim 10^6$ depending on the chosen resolution. For nonlinear Bayesian inverse problems, Markov Chain Monte Carlo (MCMC) sampling methods are commonly used for parameter estimations, but performing this method repeatedly at all the grid points is computationally expensive. To address this computational difficulty, we use an alternative and equivalent form of the vertical displacement model

$$w^{\hat{u}}(\mathbf{r}, t) = A(\mathbf{r}) \max(\sum_{\xi} \tilde{a}_i \sin(\omega_\xi t + \phi_\xi), K'(\mathbf{r})) \tag{41}$$

$$K(\mathbf{r}) = A(\mathbf{r}) K'(\mathbf{r}) \tag{42}$$

In the original form (equation 41), there are two parameters $A(\mathbf{r})$ and $K(\mathbf{r})$ in the max operator. In this alternative form, $A(\mathbf{r})$ is moved outside of the max operator leaving $K'(\mathbf{r})$ to be the only nonlinear parameter. Once $K'(\mathbf{r})$ is fixed, we can solve for the remaining parameters efficiently using the closed-form solutions for linear problem. Thus, we take the following approach to solve the nonlinear inverse problem:

1. Discretize K' with a sampling interval significantly smaller than its intrinsic uncertainty (e.g., 1 cm). We denote the n enumerated values as $K'^{(i)}$, where $i = 1, 2, ..., n$.

2. For every $K'^{(i)}$, solve for remaining parameters and obtain the corresponding model likelihood $P^{(i)}(K'|\mathbf{d})$.

3. The index of the optimal model is $s = \text{argmax}(P^{(i)}(K'|\mathbf{d}), i = 1, 2, \cdots, n)$ and the corresponding optimal enumerated ephemeral grounding level is $K'^{(s)}$. Using the equation (42), we get the optimal grounding level K.

4. We obtain the approximate posterior marginal probability distribution of K' from $P^{(i)}(K'|\mathbf{d})$, where $i = 1, 2, \cdots, n$. The marginal distribution quantifies the uncertainty in estimated K' and informs whether the ephemeral grounding level is well constrained.

The revision in the formulation of the inverse problem after introducing K' can be arrived at naturally by plugging equation (41) into equation (35). We describe the revised formulation in the supporting information Text S2.

Besides the computational efficiency, introducing K' has the advantage that it normalizes the ephemeral grounding level in the problem with respect to the amplitude. Clipping on the tidal displacement without amplitude scaling $A(\mathbf{r})$, K' is the normalized version of K, such that it is not sensitive to the amplitude of tidal displacement. The distribution of K' is advantageous over K in evaluating the existence and uncertainty in ephemeral grounding, because a consistent criterion, for example, the threshold of determining the existence of grounding, can be used in both large and small tidal amplitude scenarios. This advantage can also be viewed as K' automatically scaling the range and sampling interval in the enumeration of grounding level with the amplitude of tidal displacement. Hereafter, unless mentioned explicitly, the distribution and statistics related to ephemeral grounding are all referred to K'.

The linearization of the original nonlinear inverse problem guarantees the solution to be optimal and enables efficiently solving the problem accelerating the computation by many orders of magnitude compared with applying MCMC sampling methods. Although there is the disadvantage that the solution is approximate due to the discretization of K', we can reduce this approximation error to be significantly smaller than the intrinsic uncertainty in the parameters by refining the discretization around the optimum.

3.4.5 Tests with Synthetic Data

We test the developed model with the same synthetic RIS model in section 3.3.3. For the inference, we use the new vertical displacement model (equation 41) and follow the approach in section 3.4.4 to solve the inverse problem by enumerating K'. In the synthetic tests, we explore different strategies for enumerating K', quantifying the uncertainty, and determining the whether the ephemeral grounding exists. Our optimization strategy is as follows:

1. Discretize K' in the tidal range $[-4.0\,\mathrm{m}, 4.0\,\mathrm{m}]$ starting with the spacing at 10 cm and iteratively refine the spacing around the optimum down to 1 cm. Resolution of 1 cm is significantly smaller than the intrinsic uncertainty in K' which is typically tens of centimeters.

2. Calculate the approximate marginal posterior probability distribution of K' from enumerated $P(K'|\mathbf{d})$ and find the 68% (approximately one standard deviation of the mean) credible interval around the optimum (supporting information Text S3).

3. Jointly use the necessary condition (section 3.4.3) and adopting a threshold $\delta_{K'}$ (e.g., $\delta_{K'}$=60 cm, which corresponds to one standard deviation $\sigma_{K'} \approx 30$ cm) as the upper

bound of the 68% credible interval size of K' to define the constrained ephemeral grounding zones.

The choice of the threshold is subjective and reflects the allowed uncertainty in results. Therefore, it is difficult to justify that a specific value of $\delta_{K'}$ is optimal. In real data application, we combine results from different choices of $\delta_{K'}$ and adopt probabilistic interpretation of the results.

Figure 4 shows the result from applying the nonlinear model to synthetic data. For the vertical displacement, both the linear amplitude scaling $A(\mathbf{r})$ and grounding level $K(\mathbf{r})$ are in good agreement with the prescribed values. Comparing with the result of the linear model (Figure S3), the bias in the estimated amplitude and phase of horizontal M_{sf} displacement variation is greatly reduced.

3.5 Error Model

In both the linear model (section 3.3) and nonlinear model (section 3.4), we consider both the measurement error and modeling error. Under the assumption of Gaussian distributions for all uncertainties, we have the following relationship (e.g., Tarantola, 2005; Duputel et al., 2012)

$$\mathbf{C}_\chi = \mathbf{C}_d + \mathbf{C}_p \tag{43}$$

where $\mathbf{C}_d$ is the data measurement covariance matrix and $\mathbf{C}_p$ is the covariance matrix for modeling error, which is also referred to as prediction error.

We use cross-correlation methods to calculate displacement from SAR scenes (see section 2). The variance of the measured displacement $\mathbf{C}_d$ is estimated from the curvature of the correlation surface (Joughin, 2002) denoted as $\hat{\mathbf{C}}_d$. The modeling error $\mathbf{C}_p$ can come from multiple sources including but not limited to (1) error in amplitude and phase values of the tidal constituents used to model vertical displacement, (2) error in our assumption of the relative phase variation (equation 27), (3) error from not modeling M_f and short-period horizontal flow variability. We do not have a good prior model for $\mathbf{C}_p$.

A χ^2 residual analysis provides an empirical way to estimate $\mathbf{C}_\chi$. More specifically, the normalized misfit r_i, $r_i = (d_i - (\mathbf{Gm})_i)/\sigma_i$, should be roughly normally distributed with standard deviation one, where i is the i-th data point and σ_i is its standard deviation in the error model (e.g., Aster et al., 2018). Thus, the square of residual $d_i - (\mathbf{Gm})_i$ should be on the same scale as $\mathbf{C}_\chi$.

We denote the estimated $\mathbf{C}_\chi$ as $\hat{\mathbf{C}_\chi}$ and assume the error to be independent (i.e., $\hat{\mathbf{C}}_\chi$ is diagonal) and employ the following approach for inversion:

1. Assuming 10 cm error for all displacement data, conduct a first inversion and find the residual of each data point.

2. For the data on the same grid point, group the data points according to the observational unit, which is determined by track and range/azimuth measurement. Assuming data in the same group share the error model, calculate the error for each group using the residual from the initial inversion. The diagonal entries of $\hat{\mathbf{C}}_\chi$ are the variances of the residual in the corresponding groups.

3. Conduct a second inversion using the empirically estimated error model $\hat{\mathbf{C}}_\chi$.

We use 10 cm as the starting error model because the residual of the plain least-square solution is typically at tens of centimeters. We note that using a different value (e.g., 20 cm) will not change the inferred error model because all the data points are still equally weighted and the approach to deriving the residual remains the same.

Using this empirical approach, we have found that modeling error dominates the measurement error ($\hat{\mathbf{C}}_d \ll \hat{\mathbf{C}}_\chi$) in the inversion with real data. Our experiences with exploring $\hat{\mathbf{C}}_\chi$ shows that inclusion of modeling error and adopting the empirically estimated $\hat{\mathbf{C}}_\chi$ is important for reducing artifacts in the results and for realistic estimate of uncertainty. The consideration of modeling error is one of the key improvements from the methods in Minchew et al. (2017) where $\mathbf{C}_p$ was not considered.

4 Results

We apply both the linear model (section 3.3) and nonlinear model (section 3.4) to the ∼2500 displacement fields we produced. The two models both infer the secular velocity and horizontal displacement variation at M_{sf} period, but differ in the inference of vertical displacement. We note that in all figures, phase values are centered at the mean phase in the observational domain and converted to the unit of minutes or days based on the period of the tidal constituent. The fortnightly flow variation is shown in displacement domain.

4.1 Application of the Linear Model

We describe the inferred vertical displacements including short-period M_2, N_2, and O_1 and the key diagnostic long-period M_{sf} that reveals ephemeral grounding. We leave discussions of the inferred secular velocity and horizontal M_{sf} displacement variation in the supporting information Text S5. Note that in Minchew et al. (2017), M_2 and O_1 displacement were inferred and reported, but N_2 was not. Based on the inferred amplitude at M_2 period, we also derive an updated grounding line which has better accuracy than the existing grounding line data (Rignot et al., 2011a; Fretwell et al., 2013). We compare the updated grounding line with the existing grounding line data and demonstrate the improved accuracy in the supporting information Text S8. The coordinates of the updated grounding line is in the supporting information Dataset S1. We use this new grounding line in all the figures.

4.1.1 Semidiurnal and Diurnal Component

The spatial variability in M_2, N_2, and O_1 components are similar in terms of amplitude (Figure 5a1-c1), but the spatial variability of the phase differ from component to component (Figure 5a2-c2). The displacement amplitude of the three components in the central trunk is about 1.6 m, 0.3 m and 0.4 m, respectively. These values are consistent with the CATS2008 tidal model (Table 1). The inferred amplitude is uniform in the central trunk and decreases in the vicinity of the grounding zone sharing similar spatial patterns supporting the assumption we use in the nonlinear model that all tidal constituents share the normalized spatial variability of amplitude. The strongest feature is the circular zone about 10 km in diameter in the middle on the west margin where the amplitude is only 20% of its central trunk amplitude. The phase estimates for M_2 and N_2 lag ($\phi < 0$) by approximately 20 min within 10 km of grounding zone. The phase lag is more pronounced in the two horns of the grounding line than the ice shelf margins. O_1 does not exhibit lagging phases in the grounding zone, but has prevalent and uniform leading phase by approximately 20 min over the upstream half of the ice shelf in our observational domain. This variation of O_1 phase is likely to be spurious because it is similar in both the value and the shape to the theoretical bias in O_1 phase estimation found in our synthetic test (Figure S1). There is a zone of M_2 leading phase in the central trunk 20 km downstream of the grounding line, which is consistent with the previously reported ephemeral grounding point (Schmeltz et al., 2001). The leading phase at this known ephemeral grounding zone is consistent with our synthetic test which shows that the linear model can produce spurious leading/lagging phase because ephemeral grounding is not explicitly accounted for (Figure S3). Phase estimates at all three tidal periods show significant leading and lagging phase (leading or lagging more than

50 min) within the low-amplitude circular zone on the west margin, suggesting that this is a pronounced ephemeral grounding zone.

4.1.2 M_{sf} Component and Ephemeral Grounding

Inference of a large-amplitude vertical M_{sf} component suggests the existence of ephemeral grounding (Figure 5d1-5d2). Because this fortnightly component does not correspond to any existing tidal forcing, its phase variation does not have immediate physical meaning. Here we only focus on the amplitude map which reveals three primary ephemeral grounding zones:

A. An isolated circular zone in the central trunk 20 km downstream of the grounding line. This zone was previously reported in Schmeltz et al. (2001).

B. An approximately 5-km-wide zone along the west margin of the ice shelf, extending to the southern end of our observational domain. There is a pronounced circular zone with relatively large M_{sf} amplitude in the middle.

C. An approximately 5-km-wide and 20-km-long zone within the eastern horn of the grounding line in the vicinity of the eastern half of the U-shaped bend of the grounding line. The southern end of this zone connects to the bathymetric ridge at the corner of the grounding line that pins the grounded ice.

The detection and quantification of ephemeral grounding confirms the prior suggestion of such zones at RIS. However, we also recognize that some of the observed strong variations in the phase of vertical displacement are artifacts caused by not accounting for ephemeral grounding in the model.

4.1.3 Comparison of Tidal Model and Inference from the Linear Model

We compare our inferred amplitude and phase values of vertical displacement at M_2, N_2, and O_1 periods with the CATS2008 tidal model (Padman et al., 2002) at a reference point ($82.0°\mathrm{W}, 78.8°\mathrm{S}$) chosen to be away from the vicinity of any grounding (Figure 1b). Given the theoretical bias in our estimation from the synthetic test (section 3.3.3), we also compare the bias-corrected amplitude and phase values to the tidal model (Table 2 and 3). Although the comparison is made at one point, it is representative of the ice shelf central trunk in our observational domain because the tidal displacement is spatially uniform.

We find that the estimated amplitude and phase at all three tidal periods agree well with the tidal model. We also find that the theoretical bias in the estimation explains the relatively large difference between the estimation and the tidal model, such as the amplitude of O_1 and the phase of N_2. This comparison validates our inferred values and shows that the inferred bias in the synthetic test is realistic and can be used to adjust inferred values from the linear model.

4.2 Application of the Nonlinear Model

We now describe the inference of amplitude scaling and ephemeral grounding level using the nonlinear model. In terms of the horizontal secular velocity, our updated results agree well with Minchew et al. (2017) albeit with fewer artifacts in the vertical component. Details can be found in the supporting information Text S9. The final spatial resolution of the reported fields is determined by the processed displacement fields and is approximately 500 m. Animations showing the vertical motion (Movie S1), horizontal ice flow (Movie S2) and the centerline flow rate (Movie S3) are provided in the supporting information.

4.2.1 Construction of the Vertical Displacement Model

To apply the nonlinear model, we construct the vertical displacement model (equation 30) by jointly using the CATS2008 tidal model and the inferred vertical displacement at M_2, N_2, and O_1 periods from the linear model (section 3.4). We set the reference point $\mathbf{r}_0$ at $(82.0°\mathrm{W}, 78.8°\mathrm{S})$ (Figure 1b) where we have shown that the tidal model agrees with the bias-corrected estimation of M_2, N_2, and O_1 in both amplitude and phase (section 4.1.3). To use the results from the linear model, we correct for the bias in all inferred values using the bias inferred from the synthetic tests (supporting information Text S1). We construct the vertical displacement model following the methodology in section 3.4.1. For details, see supporting information Text S7.

4.2.2 Vertical Displacement with Ephemeral Grounding

The inferred amplitude scaling, $A(\mathbf{r})$, representing the amplitude of vertical displacement at all tidal periods, is uniform in the central trunk, gradually decreases in the vicinity of the grounding zone and is zero on the grounded ice (Figure 6a). The amplitude scaling typically decreases from 1 to 0 over distances of approximately 5 km on both the western and eastern ice shelf margins. The circular zone in the middle of ice shelf western margin has an amplitude approximately 20% the amplitude in the central trunk. Near the grounding line horns, the amplitude starts to decrease towards the U-shaped bend of grounding line and gradually decrease to zero within in the two horns (Figure 6a).

The ephemeral grounding zones are consistent with the inferred amplitude of the vertical M_{sf} component from the linear model (section 4.1.2). Here, we discuss the three primary ephemeral grounding zones (Figure 6b-c):

A. For the isolated ephemeral grounding zone in the central trunk (A), the grounding level is approximately -1.7 m at its center and gradually decreases towards the periphery. The lowest grounding level detected is approximately -2.5 m at on the northern end. As described in section 3.4.3, the inferred ephemeral grounding zone is the minimum spatial extent of the actual ephemeral grounding zone.

B. The grounding level on the western margin is relatively high, ranging from -1 m to 0 m. The northern portion (B1) is approximately 5-km-wide with the grounding level increasing towards the grounding line. The width of this zone decreases towards the south. The low-amplitude circular-zone (B2) has a relatively high grounding level near 0 m. We find no ephemeral grounding to the north and less ephemeral grounding to the south of this zone. The southern portion (B3) has a similar grounding level as the northern portion.

C. The grounding level of the ephemeral grounding zone in the eastern horn of the grounding line (C1) ranges from -0.5 m to 0 m, increasing as one approaches the grounding line. This whole zone is slightly wider than the zone on the western margin and exhibits a smaller gradient in the change of grounding level. Within the western horn of the grounding line, a small ephemeral grounding zone (C2) exists at the northern end with the level of ephemeral grounding close to 0 m.

We find the zones of ephemeral grounding primarily exist in the vicinity of the grounding zone along the western margin of RIS. The spatial distribution of zones of ephemeral grounding should reflect the current bathymetry, which we have very limited knowledge of, beneath RIS (Smith & Doake, 1994; Johnson & Smith, 1997). On the western side, the seaward slopes of the bed should be relatively small which introduce relatively wider grounding zone and more abundant existence of ephemeral grounding. On the eastern side, the bed should be steep which makes the grounding zone to be narrow and limits the existence of ephemeral grounding.

Considering the total area and the grounding level, the main ephemeral grounding zone is on the western margin (B1-B3). This zone should contribute most to the tide-modulated buttressing stress compared with other zones. That the southern portion of this zone extends to the southern end of our observational domain suggests that zones of ephemeral grounding extend further the downstream. Observations have shown that the grounded portion of the RIS upstream of the grounding line is deeper on its western margin (Fretwell et al., 2013; Morlighem et al., 2020), so the thickness of the ice shelf downstream should also be thicker on the western side. Whether the ephemeral grounding on the western margin downstream of the grounding line is caused by the increased ice-shelf thickness or variations in sub-shelf bathymetry remains an open question.

4.2.3 Horizontal Fortnightly Flow Variability

Here, we present the inferred variations in flow and the derived strain rates. In the 2-D horizontal plane, we define along-flow and cross-flow as the directions along (parallel to) and across (perpendicular to) the inferred direction of secular velocity. The cross-flow direction is 90° counter-clockwise from the along-flow direction.

This updated version of fortnightly flow is consistent with the results in Minchew et al. (2017) in terms of the major features, but has three improvement: (1) There were artifacts in Minchew et al. (2017) associated with SAR image boundaries and some extreme values caused by the instability in the inversion due to lack of data. This new version has less artifacts and thus enables deriving variations in strain rates. (2) The inferred heterogeneity of the fortnightly flow in Minchew et al. (2017) may be overestimated due to the aforementioned artifacts. Our improved version shows that the fortnightly flow has smoother spatial variation. (3) This version also better resolves the cross-flow component and shows the periodic divergence and convergence of the flow in that direction.

4.2.3.1 Variation in the Along-Flow Component

The along-flow variation is highest over the ice shelf with a peak-to-peak amplitude of approximately 80 cm and varies smoothly in space (Figure 7a). The trend of increasing amplitude downstream suggests that this variation is not limited to the observed portion of the ice shelf. The low amplitudes along the western margin should be primarily due to the low mean flow speed.

Leading phase values are present over the ice shelf (Figure 7b) and are relatively uniform. The prominent circular ephemeral grounding zone in the middle along the western margin (B2) has the most leading phase values. The isolated ephemeral grounding zone in the central trunk of the ice shelf (A) also exhibits leading phases. In addition, phase at the ice-shelf margins, where ephemeral grounding is likely to exist, generally leads the phase in the ice-shelf central trunk. All these observations suggest that ephemeral grounding plays an important role in the generation of fortnightly flow variation.

4.2.3.2 Variation in the Cross-Flow Component

The amplitude of the cross-flow variation on the ice shelf ranges from 5 cm in the central trunk to 15 cm located along the western and eastern ice shelf margins and near the U-shaped bend of the grounding line (Figure 7c). The phase of this variation is anti-symmetric with the maximum difference of phase values on the western and eastern sides at half of the fortnightly period (approximately 7.4 days). We find that the large amplitudes near the margin and anti-symmetry in phase together lead the periodic divergence and convergence of the ice flow during acceleration and deceleration (Movie RIS-H).

4.2.3.3 Variations in Strain Rate

The variation in longitudinal strain rate ($\dot{\epsilon}_{xx}(t) = \partial(v_x(t) - \bar{v}_x)/\partial x$, where x is in the along-flow direction) calculated from the fortnightly flow rate shows extension (positive value) and compression (negative value) of the ice in the along-flow direction during acceleration and deceleration (Movie RIS-H). At the centerline of RIS, the amplitude of variation is approximately $5\,\mu$/day ($\mu = 10^{-6}$). The localized high strain-rates are present at the central bathymetric ridge that pins the grounding line at the downstream extent of the U-shaped bend and near the circular zone of pronounced ephemeral grounding on the western ice-shelf margin (Figure 8 and 9). Large negative strain rates (compression) with amplitude larger than $10\,\mu$/day are present when the ice is accelerating suggesting that the ephemeral grounding provides resisting stress to ice flow.

The variation in transverse strain rate ($\dot{\epsilon}_{yy}(t) = \partial(v_y(t) - \bar{v}_y)/\partial y$ where y is in the cross-flow direction) shows the extension and compression of ice in the cross-flow direction during acceleration and deceleration which corresponds to the ice-flow divergence and convergence (Movie RIS-H). The strain rates with amplitudes of approximately $10\,\mu$/day are present in two-bands along ice-shelf flow with less variation in the center (Figure 8 and 9). Near the circular zone on the western margin where the pronounced ephemeral grounding is located, there is compression during acceleration which is presumably driven by basal pinning (Movie RIS-H).

The variation in shear strain rate ($\dot{\epsilon}_{xy}(t) = \frac{1}{2}(\partial(v_x(t) - \bar{v}_x)/\partial y + \partial(v_y(t) - \bar{v}_y)/\partial x)$ where x is in the along-flow direction and y is in the cross-flow direction) shows the dominant shear strain rate in the western and eastern margins. The strain rate along the western margin is more dispersed and has more spatial variations due to the more complicated margin geometry, ephemeral grounding, and the inflow of the Minnesota Glacier (MG) that intersects RIS (Figure 1b). The eastern grounding line horn where the more ephemeral grounding exists experiences a higher magnitude of strain rate than the western horn.

5 Discussion

5.1 Asymmetric Response to Tidal Forcing

Previous studies have suggested that the M_{sf} signal over the ice-shelf-stream at RIS is driven by the asymmetric response of ice shelf flow to the high and low tide. By studying the variation of the lateral shear strain rate, Minchew et al. (2017) proposed that the ephemeral (periodic) grounding of the ice shelf during low tide along the ice shelf margin leads to the tide-modulated contact area of the ice shelf with the bed changing the effective ice shelf width, with the resulting temporal evolution of the basal shear traction and the buttressing stress giving rise to the observed variations flow rate. Motivated by the theoretical model on the tide-modulated asymmetric grounding line migration (Tsai & Gudmundsson, 2015) and the observations of the ephemeral grounding at RIS (Schmeltz et al., 2001; Minchew et al., 2017), Robel et al. (2017) proposed that the ice shelf buttressing stress to be an asymmetric function of the tide height with the high tide corresponds more significant buttressing stress decrease than the equivalent low tide corresponds to the buttressing stress increase. Employing this buttressing stress model, they were able to reproduce the amplitude and phase of the observed fortnightly flow rate variation in a 1-D model using Maxwell viscoelastic rheology. Using extensive GPS records, S. H. R. Rosier et al. (2017) showed that this fortnightly flow rate variation is prevalent over the entire Filchner-Ronne Ice Shelf (FRIS) and all the adjoining ice streams including RIS. The amplitude of this variation increases downstream to the ice shelf front suggesting that the underlying mechanism is not particular to a certain ice stream. Using the realistic geometry of FRIS and a 3-D full Stokes viscoelastic model, Rosier and Gudmundsson (2020) were able to reproduce the amplitude of this fortnightly flow rate variation by modeling the asymmetric grounding line migration (Tsai & Gudmundsson, 2015; Minchew et al., 2017) and the nonlinear dependence of the flow rate on the ice shelf width. Warburton et al. (2020) developed a mathematical model showing that grounding line migration is dependent on the permeability and drainage speed of the subglacial hydrological system. The effective grounding line can be pinned at the point of the high tide for low-permeability system resulting in asymmetric widening and shrinking of grounding zone and leading to the fortnightly flow variability.

While all the aforementioned mechanisms point to the asymmetric response of the ice shelf flow to the tidal forcing, the observational evidence has been limited. Our study here focuses on observing the ephemeral grounding of the ice shelf, a potentially important mechanism for generating the tide-modulated buttressing (Minchew et al., 2017; Robel et al., 2017), and shows that the ephemeral grounding at RIS is not limited to the pinning point detected by Schmeltz et al. (2001), but is also present in significantly larger zones including the western ice shelf margin and the eastern grounding line horn. This observation provides direct evidence for the tide-modulated grounding of the ice shelf and provides support for mechanisms dependent on the evolution in basal shear traction. The ephemeral grounding on the western margin also suggests the existence of more ephemeral grounding downstream of our observational domain and the potential for explaining the fortnightly flow rate variation outside RIS.

5.2 Long-Term Response to Ice Shelf Thinning

The Western Antarctic Ice Sheet (WAIS) is thought to be unstable in response to the ongoing oceanic warming and ice-shelf melting (e.g., Joughin et al., 2012; Alley et al., 2015). Buttressing stress from the ice shelves plays an important role in regulating the ice-sheet discharge (e.g, Thomas, 1979; Dupont & Alley, 2005; Gudmundsson, 2013) and generating tidal variability in ice flows (e.g, Padman et al., 2018). However, with ice-shelf thinning and grounding line retreat, the resulting reduction in basal traction allows the ice flow to speed up and thin, and the grounding line to retreat, especially where the bed is prone to to a buoyancy-driven dynamical feedback known as the marine ice-sheet instability (Weertman, 1974; Schoof, 2007; Cuffey & Paterson, 2010). Such dynamic response of the ice flow to ice shelf thinning has been observed at multiple glaciers, such as Pine Island Glacier and Thwaites Glacier, along the Amundsen coast where the flow acceleration currently accounts for most of the ice discharge increase from the western Antarctica (e.g, Joughin et al., 2014; Sutterley et al., 2014; Gardner et al., 2018). Unlike the ice shelves in Amundson Sea Sector, FRIS currently has a net mass loss close to zero, resulting in almost constant ice thickness and no increase in ice discharge (e.g., Pritchard et al., 2012; Paolo et al., 2015). However, studies have shown that sub-shelf ocean currents below FRIS could transition from cold to warm by the end of the century increasing the basal melting by more than a order of magnitude (Hellmer et al., 2012). Such change can lead to decrease of the buttressing stress and increase outflows from the adjoining ice streams, and potentially removing large portions of WAIS.

The tide-induced ephemeral grounding is the intermediate state between persistently grounded and persistently ungrounded states. Compared with persistent pinning points, the buttressing effect of the ephemeral grounding zones is more sensitive to ice-shelf thinning which causes immediate shrinkage of the grounding zone area and the further transition into an ungrounded state. Thus, quantifying the buttressing effect of the ephemeral grounding zone and the loss of the buttressing due to ice-shelf thinning is important for predicting the future response of Antarctic glaciers to oceanic warming and ice shelf thinning.

The secular loss of this buttressing should in turn be compensated for by increased drag upstream. Given a decrease in buttressing stress (an increase in longitudinal stress $\Delta\tau_{xx}$), we develop an simple model to quantify the increase in ice flow rate (see Appendix A):

$$\Delta u = \frac{2nu_c}{\rho g \alpha L}\Delta\tau_{xx}. \tag{44}$$

where $\Delta\tau_{xx}$ is the change in longitudinal strain rate (stress in taken to be positive in extension), L is a characteristic length scale for RIS, u_c is the centerline velocity, α is the surface slope for the ice-shelf portion of RIS, n is the exponent in Glen's flow law, ρ is the mass density of ice, g is the gravitational acceleration.

We can estimate current variations in longitudinal stress using the measured flow variability. Using a laterally confined ice stream model, we developed a theoretical model characterizing the relationship between the variation in longitudinal stress and the variation in velocity (see supporting information Text S10). Using this relationship, we estimate the variation in longitudinal stress to be approximately 75 kPa. Assuming that the current tide-induced buttressing stress variation is mainly associated with the sub-shelf bathymetry and can be largely reduced by the future ice-shelf thinning, the current variation in longitudinal stress is the lower bound of the decrease in longitudinal stress. Thus, we can use 75 kPa in equation (44) and the obtain an estimate of the increase in ice flow rate to be approximately 1 m/d at RIS, in other words, a doubling speed of the the present-day 1 m/d characteristic flow speed (see Appendix B).

5.3 Mapping Ephemeral Grounding Zone with SAR Observations

We demonstrate a methodology for identifying uncharted ephemeral grounding zones and quantifing the grounding level using temporally dense SAR observations. The identification of sub-shelf pinning points has previously relied on the detection of surface elevation changes, including ice rises and ice rumples, using satellite imagery (e.g., Scambos et al., 2007; Matsuoka et al., 2015). Feature tracking on synthetic aperture radar and optical images can reveal modulated ice flow by the pinning points (e.g., Rignot, 2002). Because ephemeral grounding does not introduce significant surface expression or modulated ice flow that traditional approaches rely on, there has not been comprehensive documentation of ephemeral grounding zones. The few observations of ephemeral grounding are limited to the ephemeral grounding points in the ice shelf central trunk which can be are revealed by the localized "bull's eye" patterns in the interferograms (e.g., Schmeltz et al., 2001; Milillo et al., 2019). However, this approach does not work well for detecting ephemeral grounding in the vicinity of the grounding zone or large regions devoid of localized patterns in the radar data.

The key characteristic that determines the capability of SAR observations on constraining the ephemeral grounding is how much and how well we sample low tide. The sampling is determined by the SAR acquisition times and the corresponding tidal displacement. Analysis of the suite of observations at RIS reveals the lowest sampled tide at any spatial point and shows that different tracks have different sensitivity to low tides (Figure 10). Because of the periodic nature of tides, the efficacy of any future the future observation campaign for study ephemeral grounding can be easily evaluated and optimized in the planning stage.

6 Conclusions

Building upon the linear geodetic model for inferring 3-D surface velocity variations from temporally dense SAR observations (Minchew et al., 2017), we fuse information from a tidal model and satellite observations to develop a new nonlinear geodetic model which simultaneously infers variations in the 3-D displacement field and tide-induced ephemeral grounding. With the increasing availability of temporally dense satellite observation (e.g., the Sentinel-1 mission, the NASA-ISRO SAR mission), the developed geodetic model for constraining the ephemeral grounding demonstrates the possibility of studying more complex (e.g., nonlinear) temporally-dependent displacement variations. The special case of tidal phenomenon also reveals the limitations of integer-day repeating times, as widely employed by space-borne SAR missions and motivates planning more observations with flexibility in choosing repeat-pass time intervals.

Our study at RIS improves on the previous result in Minchew et al. (2017) and explicitly identifies ephemeral grounding zones. The inferred ephemeral grounding zones provide new observational evidence for the asymmetric response of the ice-shelf flow to the high and low tides, which is a key component in all proposed mechanisms for generating the observed fortnightly flow variability. With continued oceanic warming and ice-shelf thinning, the loss of this ephemeral grounding will decrease buttressing stress. For RIS, we estimate that just the loss of the presently identified ephemeral grounding zones will result in at least a doubling of ice flux. Actual increases would presumably be larger as some fully grounded regions will become ephemeral as the ice thins.

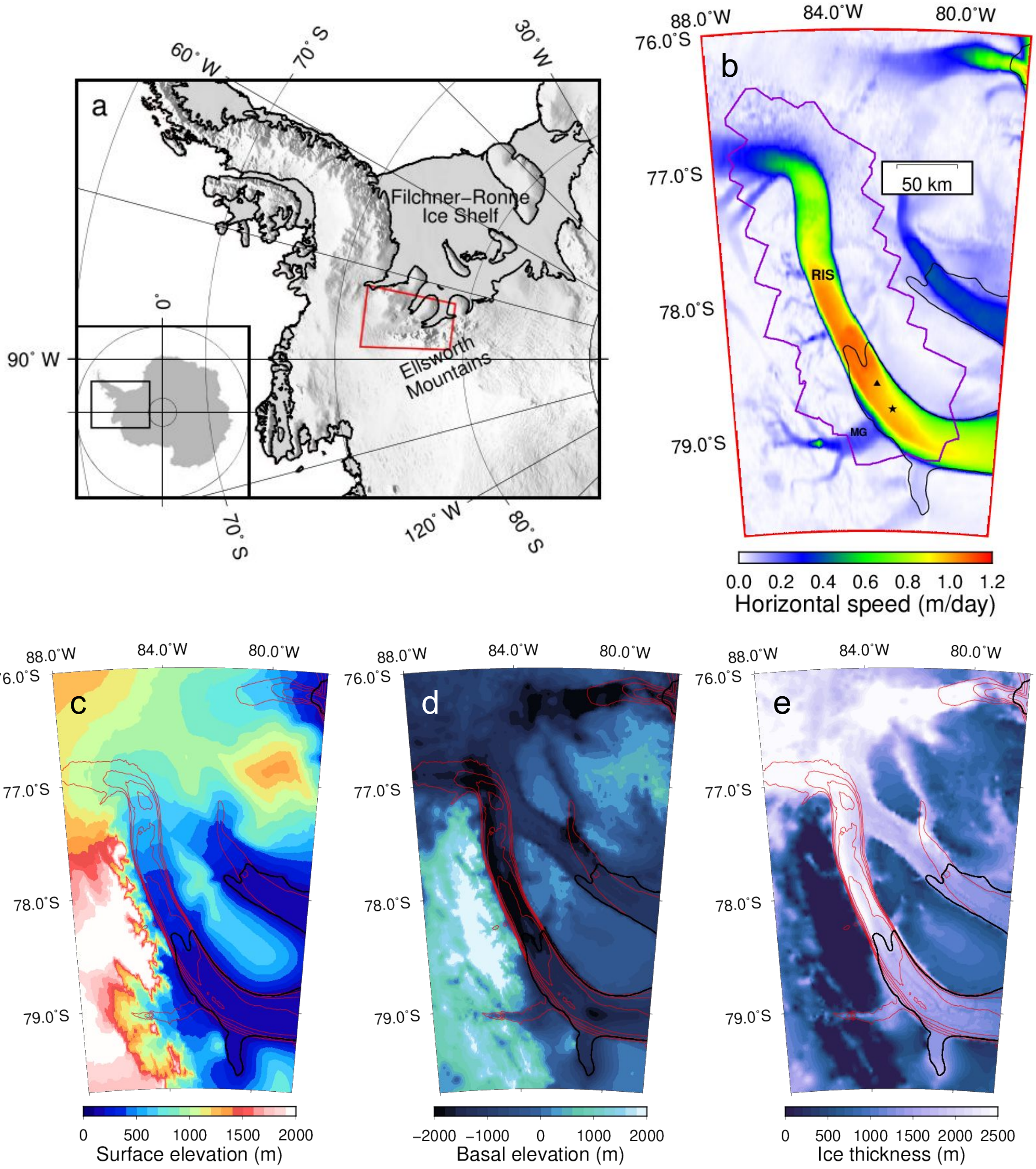
a
60° W
70° S
30° W
Filchner–Ronne Ice Shelf
Ellsworth Mountains
90° W
0°
120° W
70° S
80° S
b
88.0°W
84.0°W
80.0°W
76.0°S
77.0°S
78.0°S
79.0°S
50 km
RIS
MG
0.0 0.2 0.4 0.6 0.8 1.0 1.2
Horizontal speed (m/day)
c
d
e
0 500 1000 1500 2000
Surface elevation (m)
−2000 −1000 0 1000 2000
Basal elevation (m)
0 500 1000 1500 2000 2500
Ice thickness (m)

Figure 1: (a) Shaded relief map of RIS and surrounding area. Red box indicates the region shown in Figures 1b–1e. (b) Horizontal velocity from Mouginot et al. (2012). Purple outline indicates the extent of the CSK observations used in this study. The black star and triangle in the ice shelf central trunk indicate the reference point used in our study and the ephemeral grounding point reported in Schmeltz et al. (2001), respectively. MG indicates Minnesota Glacier flowing into RIS. (c and d) Surface and basal elevation relative to mean sea level. (e) Ice thickness. Red contour lines in Figures 1c–1e indicate horizontal surface velocity from Figure 1b in 0.2 m/d increments. In all panels, irregular black lines indicate the grounding line. All the elevation data is from BedMachine V2 (Morlighem et al., 2020). In all panels, irregular black lines indicate grounding line from Bedmap2 (Fretwell et al., 2013). This figure is adapted from Figure 1 in Minchew et al. (2017) with updates of elevation data from Bedmap2 to BedMachine V2.

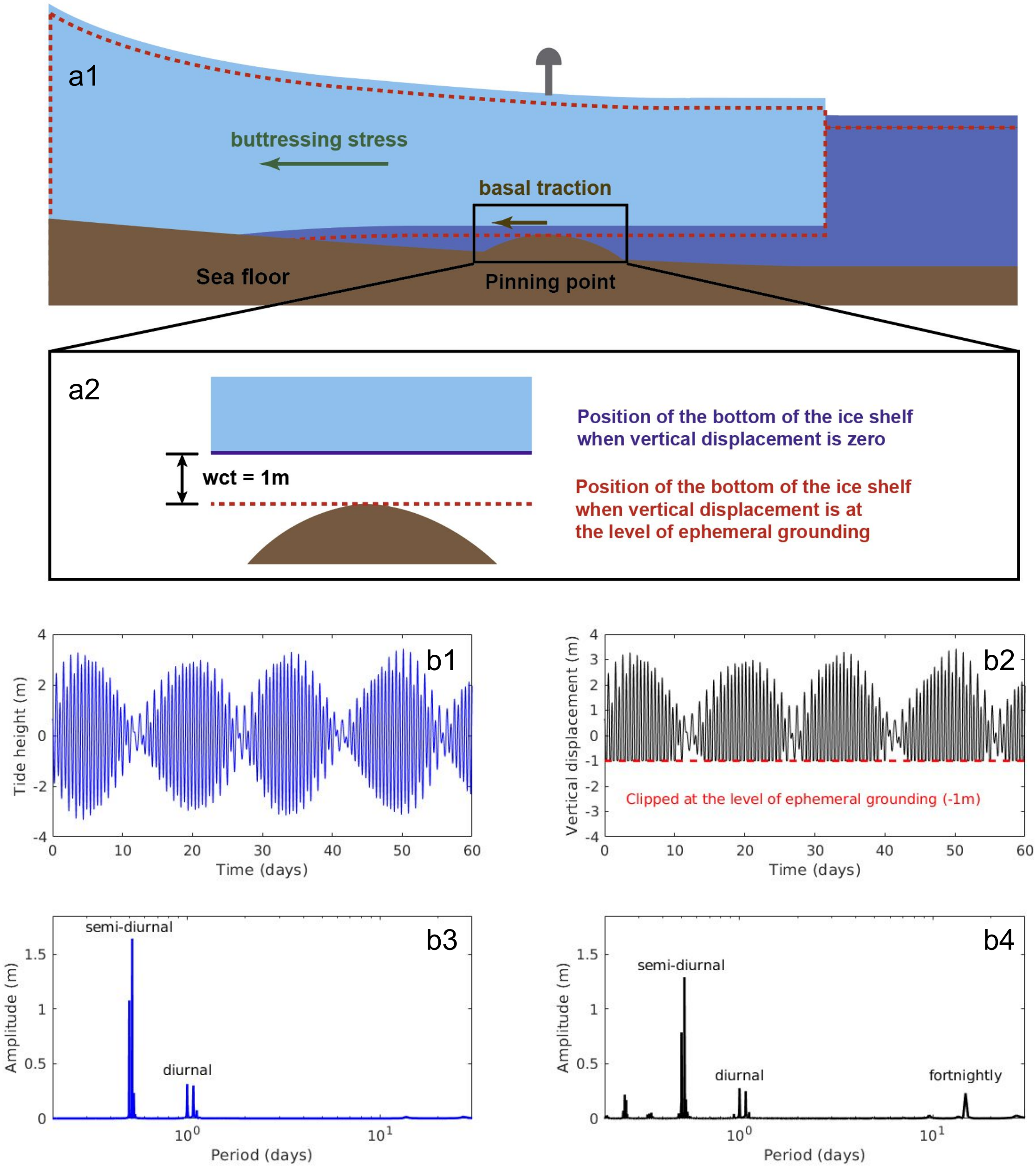
a1
buttressing stress
basal traction
Sea floor
Pinning point
a2
wct = 1m
Position of the bottom of the ice shelf
when vertical displacement is zero
Position of the bottom of the ice shelf
when vertical displacement is at
the level of ephemeral grounding
b1
Tide height (m)
Time (days)
b2
Vertical displacement (m)
Clipped at the level of ephemeral grounding (-1m)
Time (days)
b3
semi-diurnal
diurnal
Amplitude (m)
Period (days)
b4
semi-diurnal
diurnal
fortnightly
Amplitude (m)
Period (days)

Figure 2: (a1) Schematic view of tide-induced ephemeral grounding on a sub-shelf pinning point. The red dashed line indicates the location of the ice shelf in hydrostatic balance with the ocean during at the level of ephemeral grounding. The brown arrow indicates the basal traction induced by the ephemeral grounding. The green arrow indicates the ice shelf buttressing stress. (a2) The level of the bottom of ice shelf when tide height is at mean sea level (solid blue) and at the level of ephemeral grounding (dashed red). (b1) Tidal height at RIS from the CATS2008 tidal model at a reference point in the central trunk (Figure 1b). (b2) Vertical displacement at the point indicated by the gray GPS station which is at the surface point of the shown sub-shelf pinning point. The level of clipping induced by ephemeral grounding is $-1\,\mathrm{m}$, which is defined as the level of ephemeral grounding. (b3-b4) Amplitude spectrum of the time series of displacement in b1 and b2 respectively.

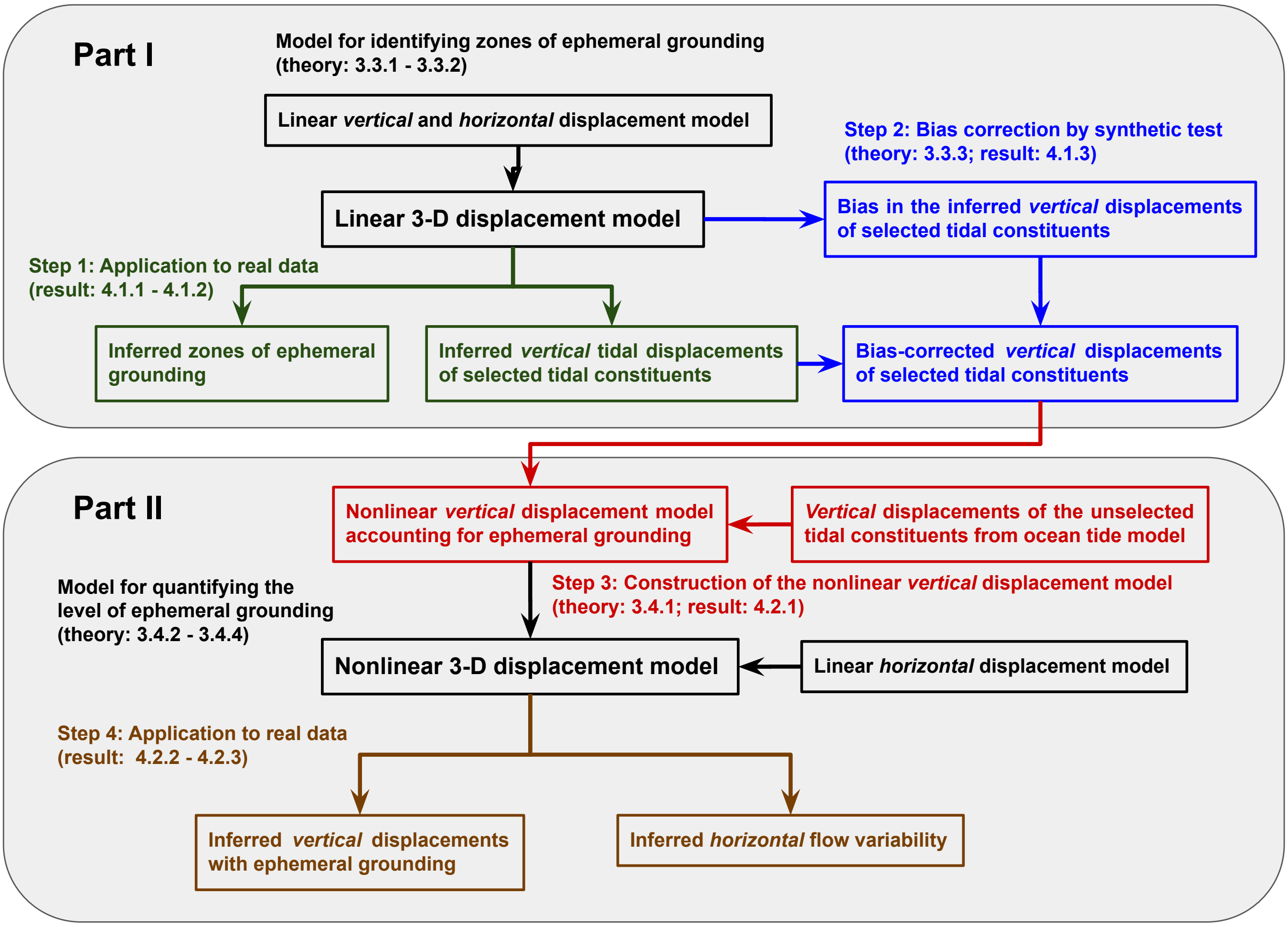

Figure 3: Outline of the workflow described herein. The workflow has two parts which are associated with a linear 3-D displacement model in the upper panel and the a nonlinear 3-D displacement model in the lower panel, respectively. The full workflow consists of the two models and four steps. For each model and step, we direct the corresponding section numbers in this paper.

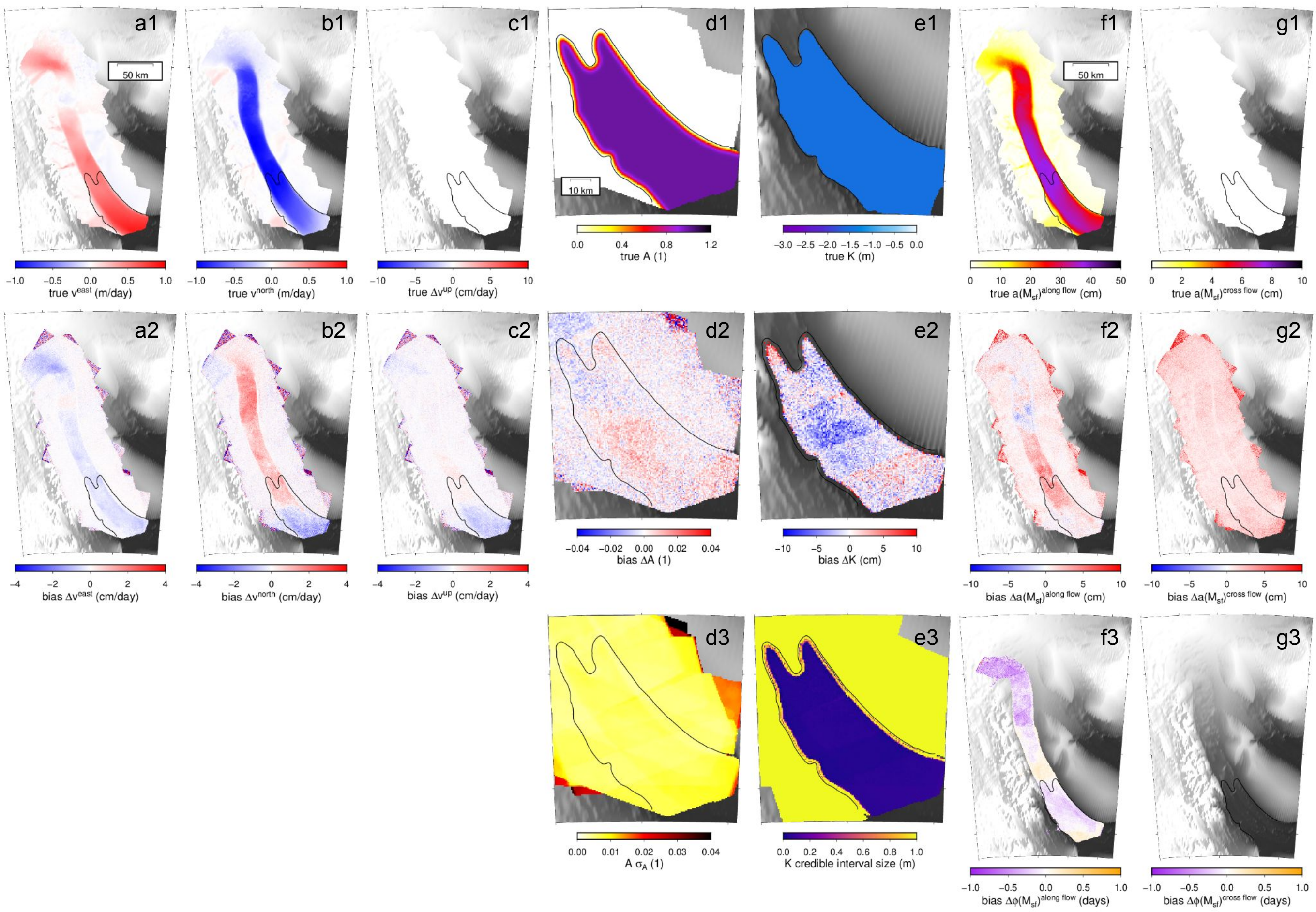

Figure 4: Results of synthetic tests. Input and bias of estimated secular velocity and tide-induced displacement using the nonlinear model assuming the seafloor is 1.5 m beneath the mean level of ice-shelf base. (a1-c1) Input horizontal and vertical secular velocity. (d1) Input vertical amplitude scaling. (e1) Input ephemeral grounding level. (f1-g1) Input horizontal sinusoidal displacement at M_{sf} period. (a2-c2) Bias of estimated secular velocity. (d2) Bias of estimated vertical amplitude scaling. (e2) Bias of estimated ephemeral grounding level. Grounding level values with the credible interval size smaller than 50 cm is shown. (d3) Formal error (1-σ) of vertical amplitude scaling. (e3) Credible interval (68%) size of the posterior probability distribution of grounding level. (f2-g2) Bias of estimated amplitude of horizontal displacement. (f3) Bias of estimated phase of horizontal sinusoidal displacement. (g3) Bias in estimated phase for cross-flow M_{sf} is not available because the input phase is undefined due to zero amplitude. The background is shaded surface elevation from Morlighem et al. (2020).

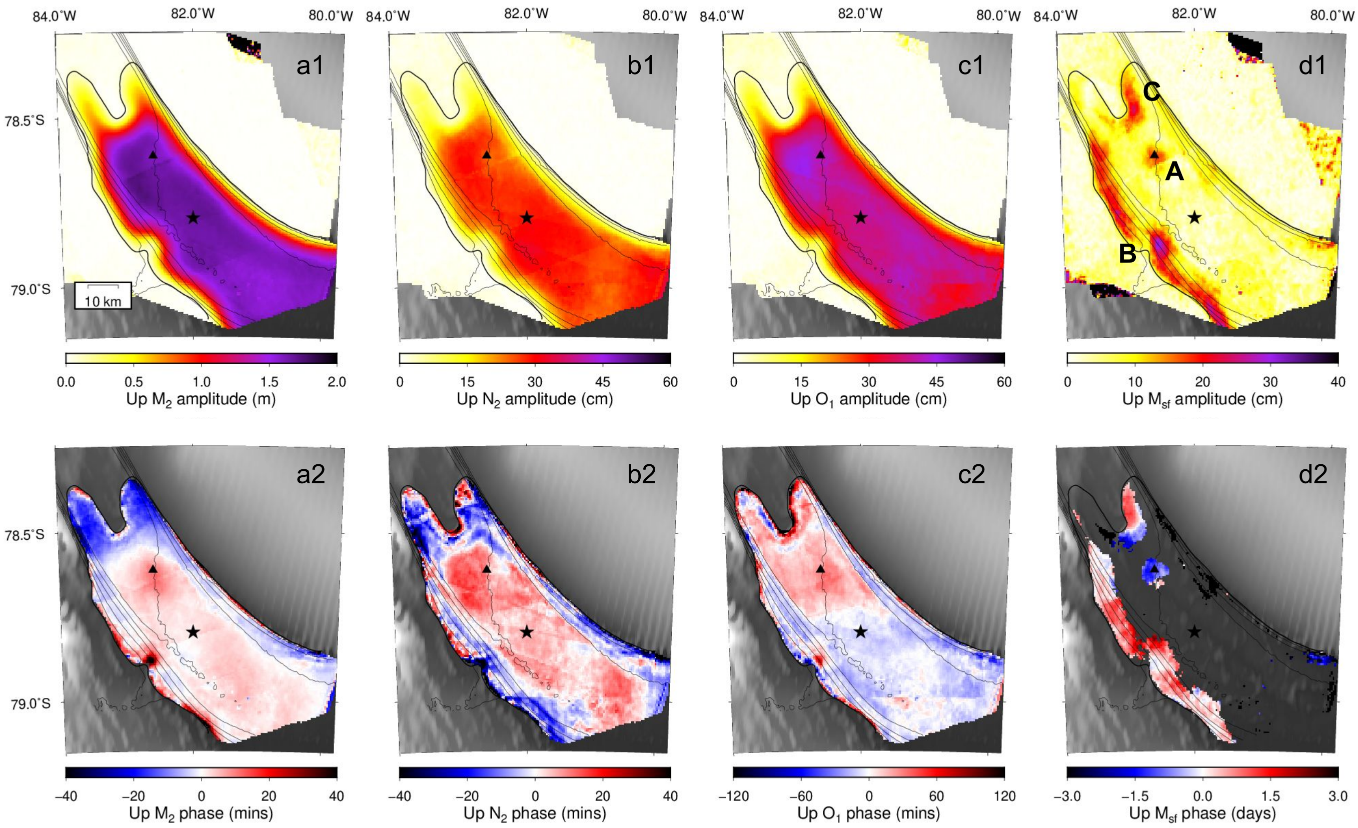

Figure 5: The tide-induced vertical displacement variation at M_2, N_2, O_1, and M_{sf} periods. (a1-d1) Amplitude variations of the vertical displacement. (a2-d2) Phase variations of the vertical displacement centered at the mean phase. Phase estimates with small amplitude ($<$ 10 cm) are not shown. Grounding lines are derived from the amplitude of M_2 using the 5 cm amplitude contour. Black star and triangle indicate the reference point and the ephemeral grounding point reported in Schmeltz et al. (2001). Black contour lines are inferred horizontal speed in 0.2 m/d increments. The background is shaded surface elevation from Morlighem et al. (2020).

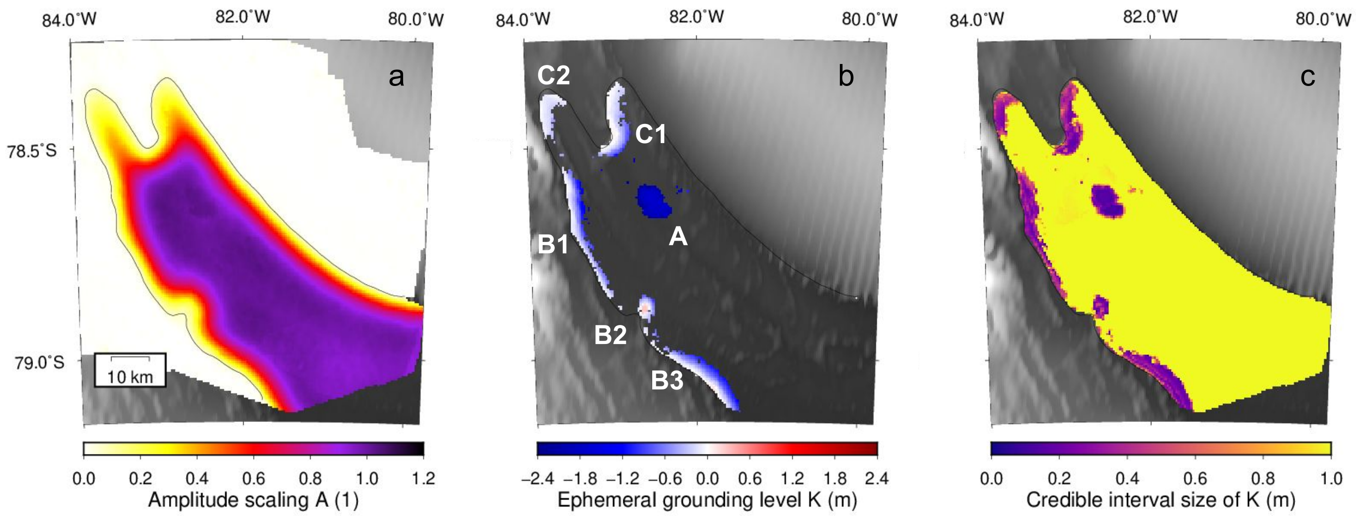

Figure 6: Vertical displacement inferred from the nonlinear model. (a) Amplitude scaling $A(\mathbf{r})$ for all constituents. (b) Ephemeral grounding level $K(\mathbf{r})$. Estimated values with credible interval size $< 80\,\mathrm{cm}$ are shown. The inferred ephemeral grounding from using a different upper bound of credible interval size are shown in Figure S13. (c) The credible interval size of the normalized ephemeral grounding level. Black contour lines are inferred horizontal speed in $0.2\,\mathrm{m/d}$ increments. The background is shaded surface elevation from Morlighem et al. (2020).

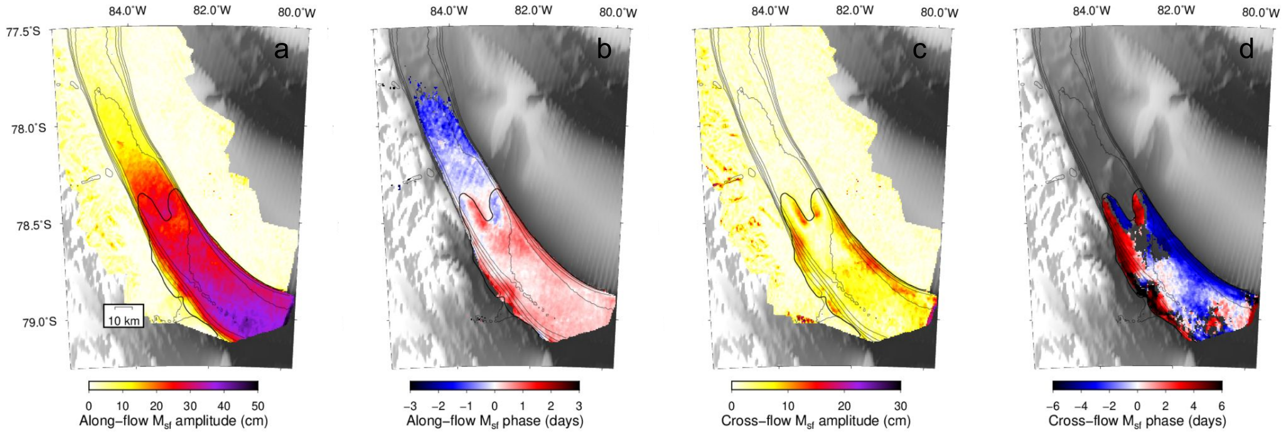

Figure 7: Along-flow and cross-flow horizontal displacements at M_{sf} (14.77 day) period. (a) Amplitude of the along-flow displacement. (b) Phase of the along-flow displacement. (c) Amplitude of the cross-flow displacement. (d) Phase of the cross-flow displacement. Black contour lines are inferred horizontal speed in 0.2 m/d increments. The background is shaded surface elevation from Morlighem et al. (2020).

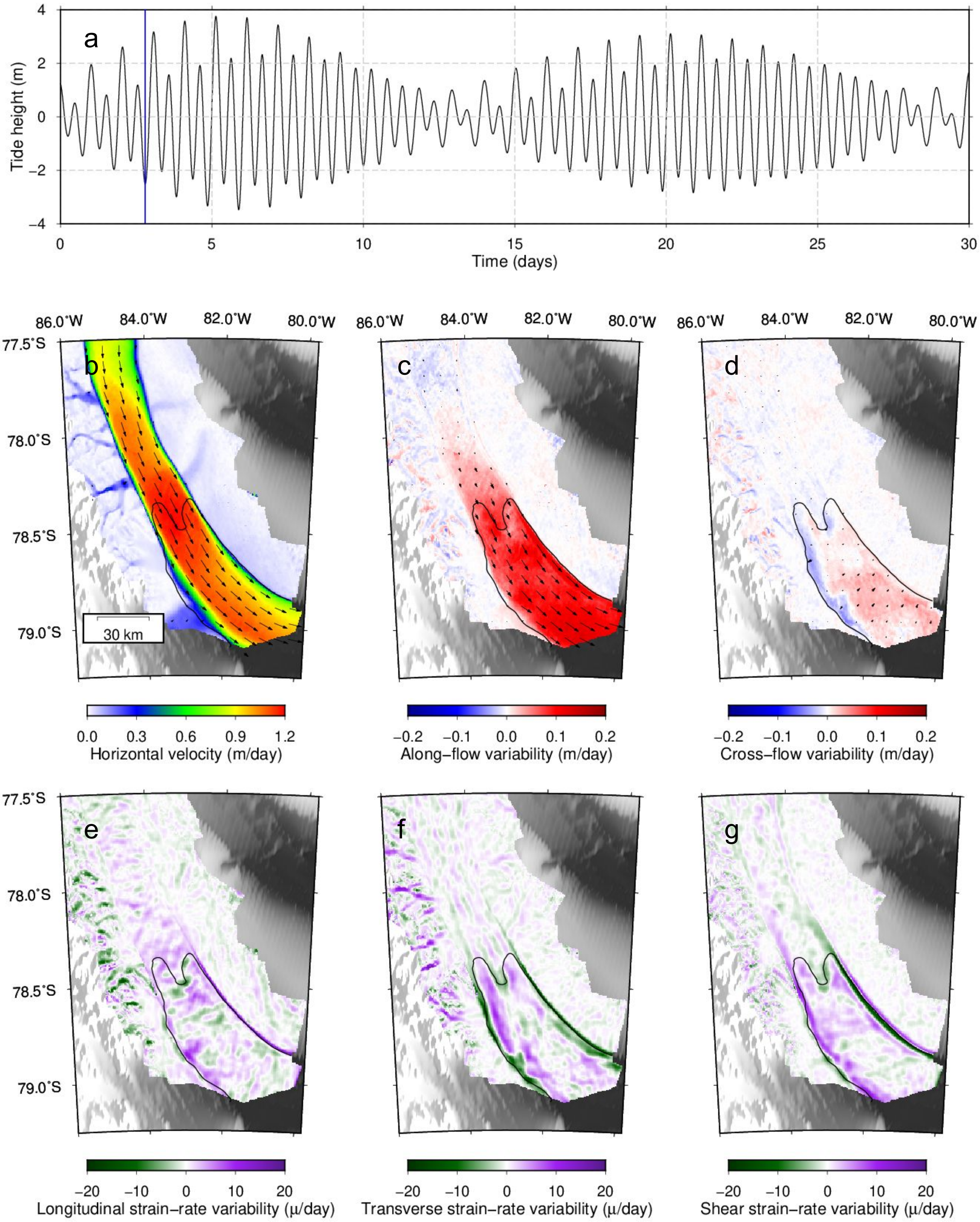
a
Tide height (m)
Time (days)
b
c
d
e
f
g
86.0°W
84.0°W
82.0°W
80.0°W
77.5°S
78.0°S
78.5°S
79.0°S
30 km
Horizontal velocity (m/day)
Along−flow variability (m/day)
Cross−flow variability (m/day)
Longitudinal strain−rate variability (μ/day)
Transverse strain−rate variability (μ/day)
Shear strain−rate variability (μ/day)

Figure 8: A snapshot of tide-induced velocity and strain rate variation (according to the definition in the main text) during flow acceleration (secular velocity removed). (a) Tidal displacement at the reference point in the central trunk where the red line indicates time of the snapshot. (b-d) Variation in ice flow velocity. (e-g) Variations in strain rate (secular component is removed). (b) Total velocity variation. Color indicates the flow speed. Arrows indicate direction and scale with speed. (c) Along-flow velocity. Arrows indicate the along-flow direction whose sizes scale with the speed. The big arrow indicates the direction of secular flow. (d) Cross-flow velocity. Arrows indicate the cross-flow variation whose sizes scale with the speed. (e) Variation in longitudinal strain rate. (f) Variation in transverse strain rate. (g) Variation in shear strain rate. The background is shaded surface elevation from Morlighem et al. (2020).

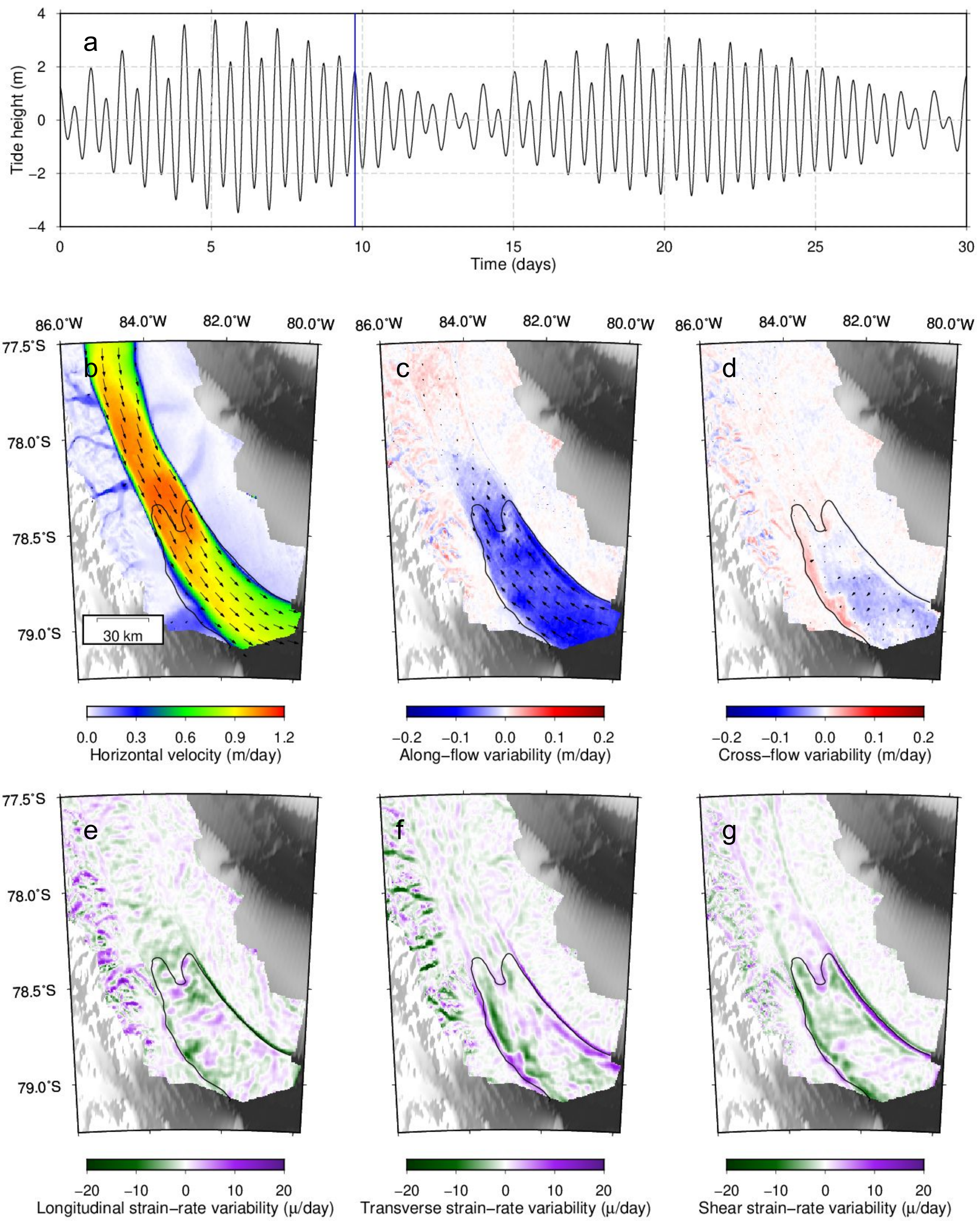

Figure 9: A snapshot during flow deceleration. The layout of panels is the same as in Figure 8.

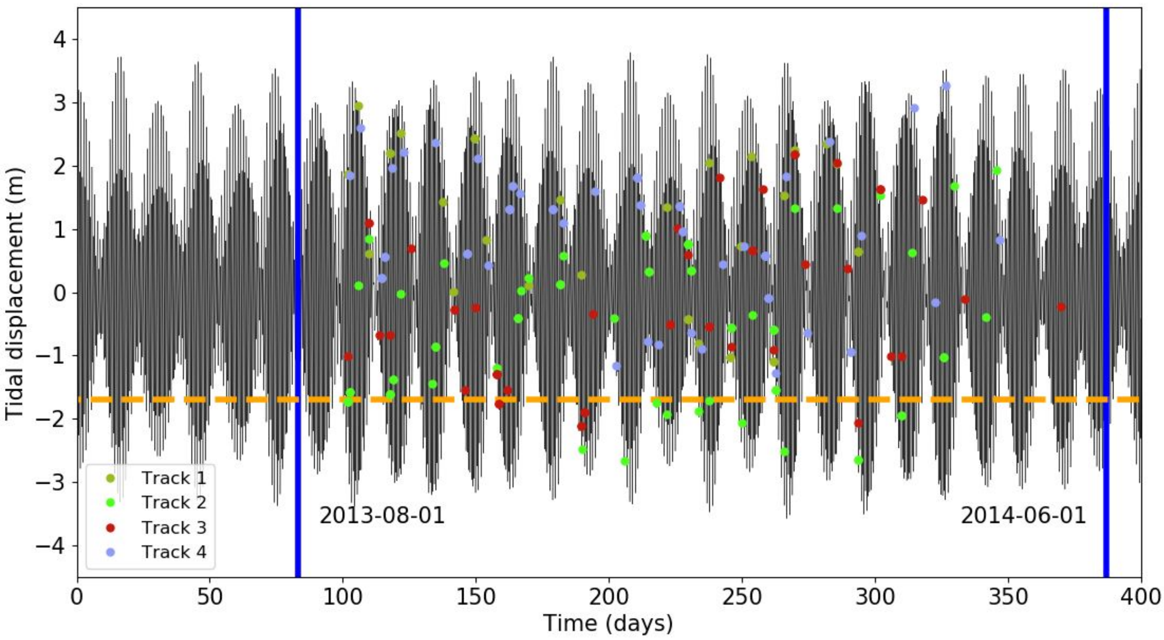

Figure 10: Tidal displacement time series (CATS2008 tidal model) and the temporal sampling of the SAR observations, sampled at the ephemeral grounding point in the central trunk where the inferred level of ephemeral grounding is approximately $-1.7\,\mathrm{m}$ (A in Figure 6b). Each SAR acquisition is shown at its timing and corresponding tide height. Colors indicate observations from different satellite ground tracks. The dashed orange line indicates the inferred level of ephemeral grounding. The two blue lines indicate the approximate start and end of the observation campaign.

Constituent	Period (days)	Reference Amplitude (m)	Reference Phase (°)	Inferred Amplitude (m)	Inferred Phase (°)
M_2	0.5175	1.647	120.69	1.666	119.63
S_2	0.5000	1.087	-10.82	-	-
N_2	0.5274	0.277	24.60	0.278	25.00
K_2	0.4986	0.238	-162.11	-	-
K_1	0.9973	0.374	36.99	-	-
O_1	1.0758	0.352	113.82	0.368	112.65
P_1	1.0027	0.140	12.92	-	-
Q_1	1.1195	0.079	10.72	-	-
M_f	13.6608	0.020	5.32	-	-
M_m	27.5546	0.017	11.99	-	-

Table 1: Reference amplitude and phase values from the CATS2008 tidal model at the reference point in the central trunk of RIS. Inferred amplitude and phase values with bias-correction at the reference point are from the linear model.

Amplitude (m)

Constituent ξ	$\hat{a}(\xi)$	$\Delta\tilde{a}(\xi)$	$\tilde{a}(\xi)$ - $\hat{a}(\xi)$	$\tilde{a}(\xi)$ - $\Delta\tilde{a}(\xi)$ - $\hat{a}(\xi)$
M_2	1.647	-0.003	0.016	0.019
N_2	0.277	0.005	0.006	0.001
O_1	0.352	0.020	0.036	0.016

Table 2: Comparison of the inferred amplitude and the reference amplitude at the reference point. $\hat{a}(\xi)$: reference amplitude from the CATS2008 tidal model. $\Delta\tilde{a}(\xi)$: estimated bias in the inferred amplitude. $\tilde{a}(\xi) - \hat{a}(\xi)$: difference between inferred amplitude and reference amplitude. $\tilde{a}(\xi) - \Delta\tilde{a}(\xi) - \hat{a}(\xi)$: difference between bias-corrected inferred amplitude and reference amplitude.

Phase (°)

Constituent ξ	$\hat{\phi}(\xi)$	$\Delta\tilde{\phi}(\xi)$	$\tilde{\phi}(\xi)$ - $\hat{\phi}(\xi)$	$\tilde{\phi}(\xi)$ - $\Delta\tilde{\phi}(\xi)$ - $\hat{\phi}(\xi)$
M_2	120.69	0.29	-0.77	-1.06
N_2	24.60	7.27	7.66	0.40
O_1	113.82	1.95	0.77	-1.17

Table 3: Comparison of the inferred phase and the reference phase at the reference point. $\hat{\phi}(\xi)$: reference phase from the CATS2008 tidal model. $\Delta\tilde{\phi}(\xi)$ estimated bias in inferred phase. $\tilde{\phi}(\xi) - \hat{\phi}(\xi)$: difference between inferred phase and reference phase. $\tilde{\phi}(\xi) - \Delta\tilde{\phi}(\xi) - \hat{\phi}(\xi)$: difference between bias-corrected inferred phase and reference phase.

Appendices

Appendix A Response of an idealized floating ice stream to changes in longitudinal stress

We derive a simple model to characterize the change in ice-shelf flow rate to change in longitudinal stress for RIS. We adopt depth- and width-averaged momentum equations for ice shelves (free slip at the base such that basal drag $\tau_b = 0$), assuming ice thickness h varies only in the along-flow (x) direction ($\partial h/\partial y \approx 0$, where y is the cross-flow direction) (Pegler, 2018)

$$-2\frac{\partial}{\partial x}(h\tau_{xx}) - \frac{h}{w}\tau_{xy} = \tau_d \tag{A1}$$

where w the local half-width of the glacier, $\tau_d = \rho g h\alpha$ the gravitational driving stress (ρ: mass density of ice; g: standard gravity acceleration; α: the surface slope). The sign convention is defined such that stresses are positive in tension.

The constitutive relation is given by Glen's Flow Law as

$$2\eta\dot{\varepsilon}_{ij} = \tau_{ij} \qquad \eta = \frac{1}{2A^{1/n}}\dot{\varepsilon}_e^{\frac{1-n}{n}} \tag{A2}$$

where $\dot{\varepsilon}_e^2 = \dot{\varepsilon}_{ij}\dot{\varepsilon}_{ij}/2$ is the effective strain rate, $\dot{\varepsilon}_{ij} = (\partial u_i/\partial x_j + \partial u_j/\partial x_i)/2$ is the strain rate tensor where u_i is the velocity vector, A is the creep parameter, and n is the exponent. Denoting the centerline velocity by u_c, rearranging and approximate Equation (A1) and Equation (A2) using

$$\dot{\epsilon}_{xy} \approx -\frac{u_c}{2w} \tag{A3}$$

$$\dot{\epsilon}_e \approx \frac{u_c}{2w} \tag{A4}$$

gives

$$-2\frac{\partial}{\partial x}\left(h\tau_{xx}\right) = \tau_d - \frac{h}{2w^2}\eta u$$
$$= \tau_d - W u_c^{1/n} \tag{A5}$$

where $W = (2w)^{\frac{-1-n}{n}} h A^{-1/n}$.

Assume that we can approximate the along flow gradient such that Equation A5 becomes

$$-2\frac{h\tau_{xx}}{L} = \tau_d - W u_c^{1/n} \tag{A6}$$

where L is the length scale for RIS.

Then we have

$$\begin{aligned} u_c &= \left[\frac{\tau_d + 2\frac{h}{L}\tau_{xx}}{W}\right]^n \\ &= A(2w)^{1+n}\left(\rho g\alpha + \frac{2}{L}\tau_{xx}\right)^n \\ &= A(2w)^{1+n}(\rho g\alpha)^n\left(1 + \frac{2}{\rho g\alpha L}\tau_{xx}\right)^n \\ &\approx A(2w)^{1+n}(\rho g\alpha)^n\left[1 + \frac{2n}{\rho g\alpha L}\tau_{xx}\right] \end{aligned} \tag{A7}$$

where the approximation comes from the binomial approximation, given that $\tau_d \gg 2\frac{h}{L}\tau_{xx}$. Under this condition, the gradient in longitudinal stress is negligible ($\frac{2n\tau_{xx}}{\rho g\alpha L} \ll 1$), which leads to the centerline velocity

$$u_c = A(2w)^{n+1}(\rho g\alpha)^n. \tag{A8}$$

Substituting Equation (A8) into the last equation in Equation (A7), we have

$$\Delta u = \frac{2nu_c}{\rho g\alpha L}\Delta\tau_{xx}. \tag{A9}$$

which relates the increase in ice flow rate to the reduction in longitudinal stress.

Appendix B The increase in ice flow rate in response to ice shelf thinning at RIS

We adopt the simple model developed in Appendix Appendix A to estimate the increase in flow rate in response to the reduction in buttressing stress due to ice shelf thinning. The estimated reduction in buttressing stress at RIS is 75 KPa ($\tau_{xx} = 75$ KPa) (supporting information S10). The parameters we use for the estimation at RIS are as follows:

$$\begin{aligned} n &= 4 \\ \alpha &= \frac{\Delta h}{L} = \frac{70\,\mathrm{m}}{100\,\mathrm{km}} = 7 \times 10^{-4} \\ L &= 100\,\mathrm{km} \\ u_c &= 1\,\mathrm{m/d} \\ \rho &= 0.9 \times 10^3\,\mathrm{kg/m^3} \\ g &= 9.8\,\mathrm{m/s^2}. \end{aligned} \tag{B1}$$

Here, $n = 4$ refers to (Millstein et al., 2022), α is derived from BedMachine V2 (Morlighem et al., 2020) and L corresponds to the length of the floating portion of RIS in our observational domain. The estimation gives the increase in flow rate $\Delta u \approx 1.0\,\mathrm{m/d}$. Note that the estimation is not dependent on n, because $\Delta\tau_{xx}$ is inversely proportional to n.

Open Research

The velocity and displacement field components (Zhong et al., 2022) are archived at https://zenodo.org/record/6615587#.Yp1DbGDMLao.

Software used to perform feature tracking on SAR images (Zhu et al., 2022) is freely available at https://github.com/lijun99/cuAmpcor.

Software used to infer ephemeral grounding (Zhong & Simons, 2022) is freely available at https://github.com/mzzhong/fourDvel2.

Acknowledgments

We thank ASI for their efforts in making the observational campaign at Rutford Ice Stream successful and the SAR data available. We thank Andrew F. Thompson for providing helpful suggestions on revising the manuscript. B.M. acknowledges NSF-NERC awards 1853918 and 1739031.

References

Alley, R. B., Anandakrishnan, S., Christianson, K., Horgan, H. J., Muto, A., Parizek, B. R., ... Walker, R. T. (2015, may). Oceanic Forcing of Ice-Sheet Retreat: West Antarctica and More. *Annual Review of Earth and Planetary Sciences*, *43*(1), 207–231. Retrieved from http://www.annualreviews.org/doi/10.1146/annurev-earth-060614-105344 doi: 10.1146/annurev-earth-060614-105344

Cuffey, K., & Paterson, W. S. B. (2010). *The Physics of Glaciers* (4th Editio ed.). Academic Press.

Dupont, T. K., & Alley, R. B. (2005, feb). Assessment of the importance of ice-shelf buttressing to ice-sheet flow. *Geophysical Research Letters*, *32*(4), 1–4. Retrieved from https://agupubs.onlinelibrary.wiley.com/doi/full/10.1029/2004GL022024 doi: 10.1029/2004GL022024

Duputel, Z., Rivera, L., Fukahata, Y., & Kanamori, H. (2012, aug). Uncertainty estimations for seismic source inversions. *Geophysical Journal International*, *190*(2), 1243–1256. Retrieved from https://academic.oup.com/gji/article-lookup/doi/10.1111/j.1365-246X.2012.05554.x doi: 10.1111/j.1365-246X.2012.05554.x

Fattahi, H., Simons, M., & Agram, P. (2017, oct). InSAR Time-Series Estimation of the Ionospheric Phase Delay: An Extension of the Split Range-Spectrum Technique. *IEEE Transactions on Geoscience and Remote Sensing*, *55*(10), 5984–5996. Retrieved from http://ieeexplore.ieee.org/document/7987747/ doi: 10.1109/TGRS.2017.2718566

Fretwell, P., Pritchard, H. D., Vaughan, D. G., Bamber, J. L., Barrand, N. E., Bell, R., ... Zirizzotti, A. (2013, feb). Bedmap2: improved ice bed, surface and thickness datasets for Antarctica. *The Cryosphere*, *7*(1), 375–393. Retrieved from https://www.the-cryosphere.net/7/375/2013/ doi: 10.5194/tc-7-375-2013

Fricker, H. A., Coleman, R., Padman, L., Scambos, T. A., Bohlander, J., & Brunt, K. M. (2009, oct). Mapping the grounding zone of the Amery Ice Shelf, East Antarctica using InSAR, MODIS and ICESat. *Antarctic Science*, *21*(5), 515–532. Retrieved from https://doi.org/10.1017/S095410200999023X doi: 10.1017/S095410200999023X

Gardner, A. S., Moholdt, G., Scambos, T., Fahnstock, M., Ligtenberg, S., Van Den Broeke, M., & Nilsson, J. (2018, feb). Increased West Antarctic and unchanged East Antarctic ice discharge over the last 7 years. *Cryosphere*, *12*(2), 521–547. doi: 10.5194/tc-12-521-2018

Goldstein, R. M., Engelhardt, H., Kamb, B., & Frolich, R. M. (1993, dec). *Satellite radar interferometry for monitoring ice sheet motion: Application to an Antarctic ice stream* (Vol. 262) (No. 5139). American Association for the Advancement of Science. Retrieved from http://science.sciencemag.org/ doi: 10.1126/science.262.5139.1525

Gudmundsson, G. H. (2006, dec). Fortnightly variations in the flow velocity of Rutford Ice Stream, West Antarctica. *Nature*, *444*(7122), 1063–1064. Retrieved from http://www.nature.com/articles/nature05430 doi: 10.1038/nature05430

Gudmundsson, G. H. (2013, apr). Ice-shelf buttressing and the stability of marine ice sheets. *The Cryosphere*, *7*(2), 647–655. Retrieved from `https://tc.copernicus.org/articles/7/647/2013/` doi: 10.5194/tc-7-647-2013

Hellmer, H. H., Kauker, F., Timmermann, R., Determann, J., & Rae, J. (2012, may). *Twenty-first-century warming of a large Antarctic ice-shelf cavity by a redirected coastal current* (Vol. 485) (No. 7397). Nature Publishing Group. Retrieved from `https://www.nature.com/articles/nature11064https://www.nature.com/articles/nature11064/` doi: 10.1038/nature11064

Johnson, M. R., & Smith, A. M. (1997). Seabed topography under the southern and western Ronne Ice Shelf, derived from seismic surveys. *Antarctic Science*, *9*(2), 201–208. Retrieved from `https://doi.org/10.1017/S0954102097000254` doi: 10.1017/s0954102097000254

Joughin, I. (2002). Ice-sheet velocity mapping: A combined interferometric and speckle-tracking approach. *Annals of Glaciology*, *34*, 195–201. Retrieved from `https://www.cambridge.org/core.` doi: 10.3189/172756402781817978

Joughin, I., Alley, R. B., & Holland, D. M. (2012, nov). *Ice-sheet response to oceanic forcing* (Vol. 338) (No. 6111). American Association for the Advancement of Science. Retrieved from `http://science.sciencemag.org/` doi: 10.1126/science.1226481

Joughin, I., Smith, B. E., & Medley, B. (2014, may). Marine ice sheet collapse potentially under way for the thwaites glacier basin, West Antarctica. *Science*, *344*(6185), 735–738. Retrieved from `http://science.sciencemag.org/http://science.sciencemag.org/` doi: 10.1126/science.1249055

King, E. C., Pritchard, H. D., & Smith, A. M. (2016, apr). Subglacial landforms beneath Rutford Ice Stream, Antarctica: detailed bed topography from ice-penetrating radar. *Earth System Science Data*, *8*(1), 151–158. doi: 10.5194/essd-8-151-2016

Matsuoka, K., Hindmarsh, R. C., Moholdt, G., Bentley, M. J., Pritchard, H. D., Brown, J., ... Whitehouse, P. L. (2015, nov). *Antarctic ice rises and rumples: Their properties and significance for ice-sheet dynamics and evolution* (Vol. 150). Elsevier. doi: 10.1016/j.earscirev.2015.09.004

Milillo, P., Rignot, E., Rizzoli, P., Scheuchl, B., Mouginot, J., Bueso-Bello, J., & Prats-Iraola, P. (2019, jan). Heterogeneous retreat and ice melt of thwaites glacier, West Antarctica. *Science Advances*, *5*(1), eaau3433. Retrieved from `http://advances.sciencemag.org/` doi: 10.1126/sciadv.aau3433

Millstein, J. D., Minchew, B. M., & Pegler, S. S. (2022, 3). Ice viscosity is more sensitive to stress than commonly assumed. *Communications Earth & Environment 2022 3:1*, *3*, 1-7. Retrieved from `https://www.nature.com/articles/s43247-022-00385-x` doi: 10.1038/s43247-022-00385-x

Minchew, B. M., Simons, M., Riel, B., & Milillo, P. (2017, jan). Tidally induced variations in vertical and horizontal motion on Rutford Ice Stream, West Antarctica, inferred from remotely sensed observations. *Journal of Geophysical Research: Earth Surface*, *122*(1), 167–190. Retrieved from `http://doi.wiley.com/10.1002/2016JF003971` doi: 10.1002/2016JF003971

Morlighem, M., Rignot, E., Binder, T., Blankenship, D., Drews, R., Eagles, G., ... Young, D. A. (2020). Deep glacial troughs and stabilizing ridges unveiled beneath the margins of the Antarctic ice sheet. *Nature Geoscience*, *13*(2). doi: 10.1038/s41561-019-0510-8

Mouginot, J., Scheuchl, B., & Rignot, E. (2012, sep). Mapping of Ice Motion in Antarctica Using Synthetic-Aperture Radar Data. *Remote Sensing*, *4*(9), 2753–2767. Retrieved from `http://www.mdpi.com/2072-4292/4/9/2753` doi: 10.3390/rs4092753

Murray, T., Smith, A. M., King, M. A., & Weedon, G. P. (2007, sep). Ice flow modulated by tides at up to annual periods at Rutford Ice Stream, West Antarctica. *Geophysical Research Letters*, *34*(18), L18503. Retrieved from `http://doi.wiley.com/10.1029/2007GL031207` doi: 10.1029/2007GL031207

Padman, L., Fricker, H. A., Coleman, R., Howard, S., & Erofeeva, L. (2002). A new tide model for the Antarctic ice shelves and seas. *Annals of Glaciology*, *34*, 247–254. Retrieved from `https://www.cambridge.org/core.` doi: 10.3189/172756402781817752

Padman, L., Siegfried, M. R., & Fricker, H. A. (2018, mar). Ocean Tide Influences on the Antarctic and Greenland Ice Sheets. *Reviews of Geophysics*, *56*(1), 142–184. Retrieved from `https://agupubs.onlinelibrary.wiley.com/doi/full/10.1002/2016RG000546https://agupubs.onlinelibrary.wiley.com/doi/abs/10.1002/2016RG000546https://agupubs.onlinelibrary.wiley.com/doi/10.1002/2016RG000546` doi: 10.1002/2016RG000546

Paolo, F. S., Fricker, H. A., & Padman, L. (2015, apr). Volume loss from Antarctic ice shelves is accelerating. *Science*, *348*(6232), 327–331. Retrieved from `http://science.sciencemag.org/` doi: 10.1126/science.aaa0940

Pegler, S. S. (2018, 12). Marine ice sheet dynamics: The impacts of ice-shelf buttressing. *Journal of Fluid Mechanics*, *857*, 605-647. Retrieved from https://doi.org/10.1017/jfm.2018.741 doi: 10.1017/jfm.2018.741

Pritchard, H. D., Arthern, R. J., Vaughan, D. G., & Edwards, L. A. (2009, oct). Extensive dynamic thinning on the margins of the Greenland and Antarctic ice sheets. *Nature*, *461*(7266), 971–975. Retrieved from https://www.nature.com/articles/nature08471 doi: 10.1038/nature08471

Pritchard, H. D., Ligtenberg, S. R., Fricker, H. A., Vaughan, D. G., Van Den Broeke, M. R., & Padman, L. (2012, apr). Antarctic ice-sheet loss driven by basal melting of ice shelves. *Nature*, *484*(7395), 502–505. Retrieved from https://www.nature.com/articles/nature10968 doi: 10.1038/nature10968

Rignot, E. (1998, jan). Radar interferometry detection of hinge-line migration on Rutford Ice Stream and Carlson Inlet, Antarctica. *Annals of Glaciology*, *27*, 25–32. Retrieved from https://www.cambridge.org/core/product/identifier/S0260305500017171/type/journal_article doi: 10.3189/1998AoG27-1-25-32

Rignot, E. (2002). Ice-shelf changes in Pine Island Bay, Antarctica, 1947-2000. *Journal of Glaciology*, *48*(161), 247–256. Retrieved from http://terraweb.wr.usgs. doi: 10.3189/172756502781831386

Rignot, E., Mouginot, J., & Scheuchl, B. (2011a, may). Antarctic grounding line mapping from differential satellite radar interferometry. *Geophysical Research Letters*, *38*(10), n/a–n/a. Retrieved from http://doi.wiley.com/10.1029/2011GL047109 doi: 10.1029/2011GL047109

Rignot, E., Mouginot, J., & Scheuchl, B. (2011b, sep). Ice flow of the antarctic ice sheet. *Science*, *333*(6048), 1427–1430. Retrieved from www.sciencemag.org/cgi/content/full/333/6048/1423/DC1 doi: 10.1126/science.1208336

Robel, A. A., Tsai, V. C., Minchew, B., & Simons, M. (2017, apr). Tidal modulation of ice shelf buttressing stresses. In *Annals of glaciology* (Vol. 58, pp. 12–20). Cambridge University Press. Retrieved from http://creativecommons. doi: 10.1017/aog.2017.22

Rosier, & Gudmundsson. (2020, jan). Exploring mechanisms responsible for tidal modulation in flow of the Filchner-Ronne Ice Shelf. *Cryosphere*, *14*(1), 17–37. doi: 10.5194/tc-14-17-2020

Rosier, S. H. R., Gudmundsson, G. H., King, M. A., Nicholls, K. W., Makinson, K., & Corr, H. F. J. (2017, nov). Strong tidal variations in ice flow observed across the entire

Ronne Ice Shelf and adjoining ice streams. *Earth System Science Data*, *9*(2), 849–860. Retrieved from https://www.earth-syst-sci-data.net/9/849/2017/ doi: 10.5194/essd-9-849-2017

Scambos, T. A., Haran, T. M., Fahnestock, M. A., Painter, T. H., & Bohlander, J. (2007, nov). MODIS-based Mosaic of Antarctica (MOA) data sets: Continent-wide surface morphology and snow grain size. *Remote Sensing of Environment*, *111*(2), 242–257. doi: 10.1016/j.rse.2006.12.020

Schmeltz, M., Rignot, E., & MacAyeal, D. R. (2001, sep). Ephemeral grounding as a signal of ice-shelf change. *Journal of Glaciology*, *47*(156), 71–77. Retrieved from https://www.cambridge.org/core/product/identifier/S0022143000212240/type/journal_article doi: 10.3189/172756501781832502

Schoof, C. (2007, feb). Marine ice-sheet dynamics. Part 1. The case of rapid sliding. *Journal of Fluid Mechanics*, *573*, 27. Retrieved from http://www.journals.cambridge.org/abstract_S0022112006003570 doi: 10.1017/S0022112006003570

Smith, A. M., & Doake, C. S. (1994). Sea-bed depths at the mouth of Rutford Ice Stream, Antarctica. *Annals of Glaciology*, *20*, 353–356. Retrieved from https://www.cambridge.org/core. doi: 10.3189/1994aog20-1-353-356

Sutterley, T. C., Velicogna, I., Rignot, E., Mouginot, J., Flament, T., van den Broeke, M. R., … Reijmer, C. H. (2014, dec). Mass loss of the Amundsen Sea Embayment of West Antarctica from four independent techniques. *Geophysical Research Letters*, *41*(23), 8421–8428. Retrieved from https://onlinelibrary.wiley.com/doi/abs/10.1002/2014GL061940 doi: 10.1002/2014GL061940

Tarantola, A. (2005). *Inverse problem theory and methods for model parameter estimation.* Society for Industrial and Applied Mathematics. Retrieved from https://books.google.com/books/about/Inverse_Problem_Theory_and_Methods_for_M.html?id=jKeHEWtzdKgC

Thomas, R. H. (1979). The Dynamics of Marine Ice Sheets. *Journal of Glaciology*, *24*(90), 167–177. Retrieved from https://www.cambridge.org/core. doi: 10.3189/s0022143000014726

Tsai, V. C., & Gudmundsson, G. H. (2015, jul). An improved model for tidally modulated grounding-line migration. *Journal of Glaciology*, *61*(226), 216–222. Retrieved from https://www.cambridge.org/core/product/identifier/S0022143000202256/type/journal_article doi: 10.3189/2015JoG14J152

Vaughan, D. G. (1995, 4). Tidal flexure at ice shelf margins. *Journal of Geophysical Research: Solid Earth*, *100*, 6213-6224. Retrieved from http://doi.wiley.com/10.1029/94JB02467 doi: 10.1029/94JB02467

Warburton, K. L. P., Hewitt, D. R., & Neufeld, J. A. (2020, sep). Tidal Grounding-Line Migration Modulated by Subglacial Hydrology. *Geophysical Research Letters*, *47*(17), e2020GL089088. Retrieved from https://onlinelibrary.wiley.com/doi/10.1029/2020GL089088 doi: 10.1029/2020GL089088

Weertman, J. (1974, jan). Stability of the Junction of an Ice Sheet and an Ice Shelf. *Journal of Glaciology*, *13*(67), 3–11. Retrieved from https://www.cambridge.org/core/product/identifier/S0022143000023327/type/journal_article doi: 10.3189/S0022143000023327

Zhong, M., & Simons, M. (2022). *fourdvel2.* Retrieved from https://zenodo.org/record/6614439#.Ypw9C2DMLao doi: 10.5281/zenodo.6614439

Zhong, M., Simons, M., Zhu, L., & Minchew, B. (2022). *Tide-induced 3d displacement fields at rutford ice stream, west antarctica.* Retrieved from https://zenodo.org/record/6615587#.Yp1DbGDMLao doi: 10.5281/zenodo.6615587

Zhu, L., Zhong, M., & Simons, M. (2022). *Pycuampcor - amplitude cross-correlation with gpu.* Retrieved from https://zenodo.org/record/6614209#.Ypw392DMLap doi: 10.5281/zenodo.6614209